PRECESSION DAMPING AND AXIAL VELOCITY CONTROL OF A LIGHTWEIGHT REENTRY VEHICLE

by

Michael A. Marino Jr.

S.B., Aeronautics and Astronautics
Massachusetts Institute of Technology
(1987)

SUBMITTED TO THE DEPARTMENT OF AERONAUTICS AND ASTRONAUTICS
IN PARTIAL FULFILLMENT OF THE REQUIREMENTS FOR THE DEGREE OF

MASTER OF SCIENCE IN AERONAUTICS AND ASTRONAUTICS

at the

MASSACHUSETTS INSTITUTE OF TECHNOLOGY

June 5, 1989

Signature of Author _____
Department of Aeronautics and Astronautics
June 5, 1989

Certified by _____
Professor James K. Roberge
Professor, Department of Electrical Engineering and Computer Science
Thesis Supervisor

Accepted by _____
Stan E. Leigh
Technical Supervisor, MIT Lincoln Laboratory

Accepted by _____
Professor Harold Y. Wachman
Chairman, Departmental Graduate Committee

PRECESSION DAMPING AND AXIAL VELOCITY CONTROL OF A LIGHTWEIGHT REENTRY VEHICLE

by

Michael A. Marino Jr.

S.B., Aeronautics and Astronautics

Massachusetts Institute of Technology

(1987)

Submitted to the Department of Aeronautics and Astronautics on June 5, 1989
in partial fulfillment of the requirements for the Degree of
Master of Science in Aeronautics and Astronautics

Abstract

A lightweight reentry vehicle is perturbed by the deployment mechanism and by the post-boost vehicle's plume. These perturbations induce coning and axial velocity deviations on the reentry vehicle. A control system, with volume and mass constraints, is designed for removing these perturbation effects. It is comprised of four cold gas thrusters, two accelerometers, and electronics for implementing the control laws. A test apparatus was constructed to verify the system design for coning angle control. The experimental evidence supports the theoretical conclusion that the system removes the vehicle's induced coning.

Thesis Supervisor: James K. Roberge
Title: Professor, Department of Electrical Engineering and Computer Science

Technical Supervisor: Stan E. Leigh
Title: Staff Member, MIT Lincoln Laboratory

Acknowledgement

The first person I must thank is Professor Winston Markey for introducing me to the world of control systems. The year I spent as his teaching assistant proved to be one of the most valuable experiences of my education.

Thanks goes to Professor James Roberge for recommending me to seek a research assignment at Lincoln Laboratory and for being my advisor. I want to thank David Immerman for introducing me to the problem of reentry vehicle control.

Special thanks goes to Stan Leigh. His patience, guidance, and engineering experience were key to the completion of this thesis and went far beyond his duty as my thesis supervisor.

Everyone in Group 76 contributed in some manner to the successful completion of my thesis. As my group leader, Carl Much's encouragement and support made working at Lincoln Laboratory enjoyable. Thanks goes to Tony Hotz for his clear explanation of dynamic systems, Mike Johnson for loaning me the accelerometers needed for my experiment, Jim Davis for his advice on battery design, and Rob Gilgen without whom I would still be waiting for my motors to come in. I also wish to thank Leo Bernotas for allowing me to borrow his Macintosh. Many others in Group 76 have helped me along the way, whether in showing me how to use a software package or in being good friends. Thank you.

We've all heard, "Behind every good man is a woman." In my case this is true. My wife's understanding and supportiveness made life as a graduate student bearable.

Table of Contents

6

List of Figures

5 Experimental Testing

6 Conclusion

Appendix B: LREP Circuitry

Appendix C: Test Apparatus Drawings

Appendix D: Test Circuitry

Appendix E: Battery/Power System Design

List of Tables

Nomenclature

Note: all units are meter, kilogram, second, and radians unless otherwise specified.

$\mathbf{x,y,z}$	Earth-fixed coordinate system unit vectors
$\mathbf{u,v,w}$	body-fixed coordinate system unit vectors
U,V,W	linear velocity along $\mathbf{u,v,w}$ respectively
P,Q,R	angular velocity along $\mathbf{u,v,w}$ respectively
Φ,Θ,Ψ	Euler angles
Θ_c	coning angle
I_u,I_v,I_w	moment of inertia about $\mathbf{u,v,w}$ respectively
F_u,F_v,F_w	net forces along $\mathbf{u,v,w}$ respectively
M_u,M_v,M_w	net moments about $\mathbf{u,v,w}$ respectively
H	angular momentum
I_{sp}	specific impulse
m_{prop}	propellant mass
g	gravity
m	mass
t	time

Chapter 1
Introduction

Volume and mass constraints of a launch vehicle's payload limit the number of reentry vehicles (RVs) which can be deployed, simplifying the task of tracking and eliminating all the RVs. One solution is deployment of many RV replicas (called LREPs) along with the RVs. Because the LREPs have no functional purpose, they can be made small and lightweight.

There are problems with this scheme. The ejection mechanism imparts an initial moment on the LREPs and RVs, and the post-boost vehicle's plume induces both forces and moments on them. As a result of their different mass properties, RVs and LREPs exhibit different dynamic behavior when perturbed by these forces and can be differentiated by observation of their motion. A detailed analysis of these forces is provided in Chapter 2 and the governing dynamic equations are presented in Chapter 3.

The objective is to develop a system of minimal mass and volume and contained inside the LREP, which will control its attitude and axial velocity. The system presented consists of two accelerometers, a state estimator, four solenoid valves, and electronic feedback compensation. The solenoids, which are connected to a pressurized argon tank, are used to deliver the needed control forces. Details of the LREP's controller are presented in Chapter 4. The control laws which are implemented are nonlinear and system stability is proven using Lyapunov theory. The performance results are determined by numerical simulations using the full order, nonlinear equations and are presented in Chapter 4.

In addition to the theoretical results and simulations, a test apparatus was constructed to provide experimental evidence of the system's stability and raise any practical issues involved in implementation. The experimental model consists of the rotational dynamics of the LREP and includes all the details necessary for full evaluation of

the coning angle control scheme. Experimental tests demonstrated system stability and raised practical problems pertaining to the accelerometers and solenoid valves. Experimental results and their impact on the LREP's control system are discussed in Chapter 5.

Chapter 2

Design Specifications and System Parameters

The objective is to design a control system which will suppress the effects of the ejection and plume forces, while meeting packaging requirements. The discriminants of interest are axial velocity and coning angle.

2.1 System Parameters

The LREP's physical parameters, as shown in Figure 2.1.1, are [1]:

mass = 3.0 kg

spin moment of inertia = 0.244 kg·m^2

inertia ratio = 0.12

base diameter = 0.76 m

height = 1.9 m

CG location = 0.92 m (from base).
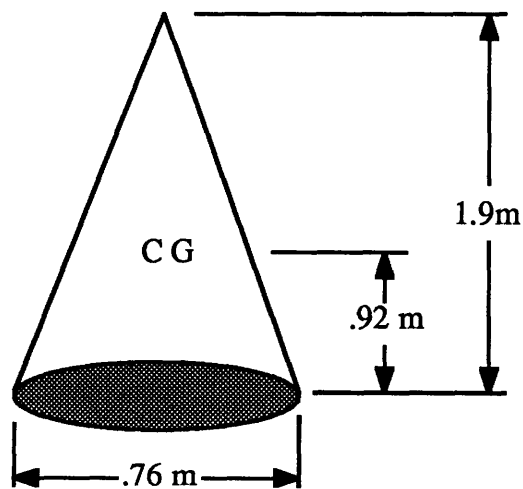
Figure 2.1.1: LREP Dimensions.

The control system's packaging requirements, which satisfy the LREP specifications given above, are [1]:

mass = 1.5 kg

height = 0.03 m

diameter = 0.76 m (cylinder).

2.2 Ejection Performance Specifications

The control system must remove the initial conditions placed on the LREP by the ejection mechanism. This mechanism inflates the LREP, rotates it to the desired spin rate of 72 deg/sec, and then ejects it off the post-boost vehicle. However, the ejection force is not coincident with the LREP's center of mass. This gives the LREP an initial tip-off rate, causing precession. Figure 2.2.1 shows the ejection force.
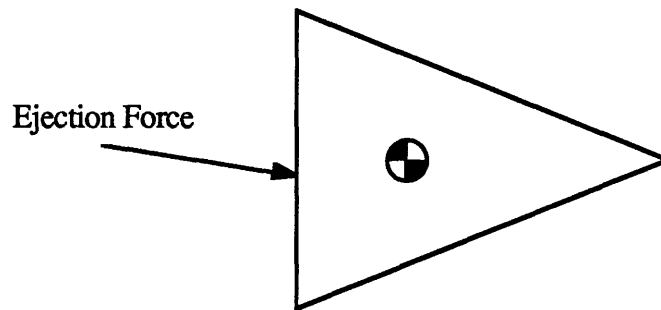
Figure 2.2.1: LREP Ejection Force.

The conditions and requirements during ejection are [1]:

ejection conditions: ejection velocity = 2.5 m/s

spin rate = 72 deg/s

tip-off rate = 3 deg/s

ejection requirements: coning half-angle = 0 deg ± 3 deg.

2.3 Plume Event Performance Specifications

The post-boost vehicle's plume induces both forces and moments on the LREP, resulting in precession and axial velocity deviations. The plume interaction does not occur immediately after ejection because there are shrouds mounted around the post-boost vehicle which initially protect the LREPs. This allows the controller to remove the initial tip-off rate before the plume event occurs. Figure 2.3.1 shows the shrouds' location. It is important to realize that there is some uncertainty as to when the plume event will occur and therefore the LREP's orientation is unknown. The assumption is made that the plume event occurs at least 1.0 sec after ejection.

There is a plume induced axial velocity change of +1.5 m/s and lateral velocity change of +0.3 m/s, for an uncontrolled 3.0 kg LREP [1]. For purposes of simulation and analysis, the induced velocities are converted to applied forces, F_{axial} and $F_{lateral}$, by

$$F_{axial} = m \frac{dv_{axial}}{dt} \qquad (2.3.1a)$$

$$F_{lateral} = m \frac{dv_{lateral}}{dt}. \qquad (2.3.1b)$$

Assuming the plume forces are exponential with a time constant, τ, of 1.25 sec, the induced disturbance forces are found by integrating Equation 2.3.1. This gives

$$\int_{t_o}^{\infty} F(t) \, dt = m \, \Delta v \qquad (2.3.2)$$

where t_o = plume interaction time. Completing the integral gives the axial and lateral disturbances for the plume event by

$$F_{axial} = 3.6 \, e^{(t_o - t)/\tau} \qquad \forall \, t > t_o \qquad (2.3.3a)$$

$$F_{lateral} = 0.72 \, e^{(t_o - t)/\tau} \qquad \forall \, t > t_o. \qquad (2.3.3b)$$
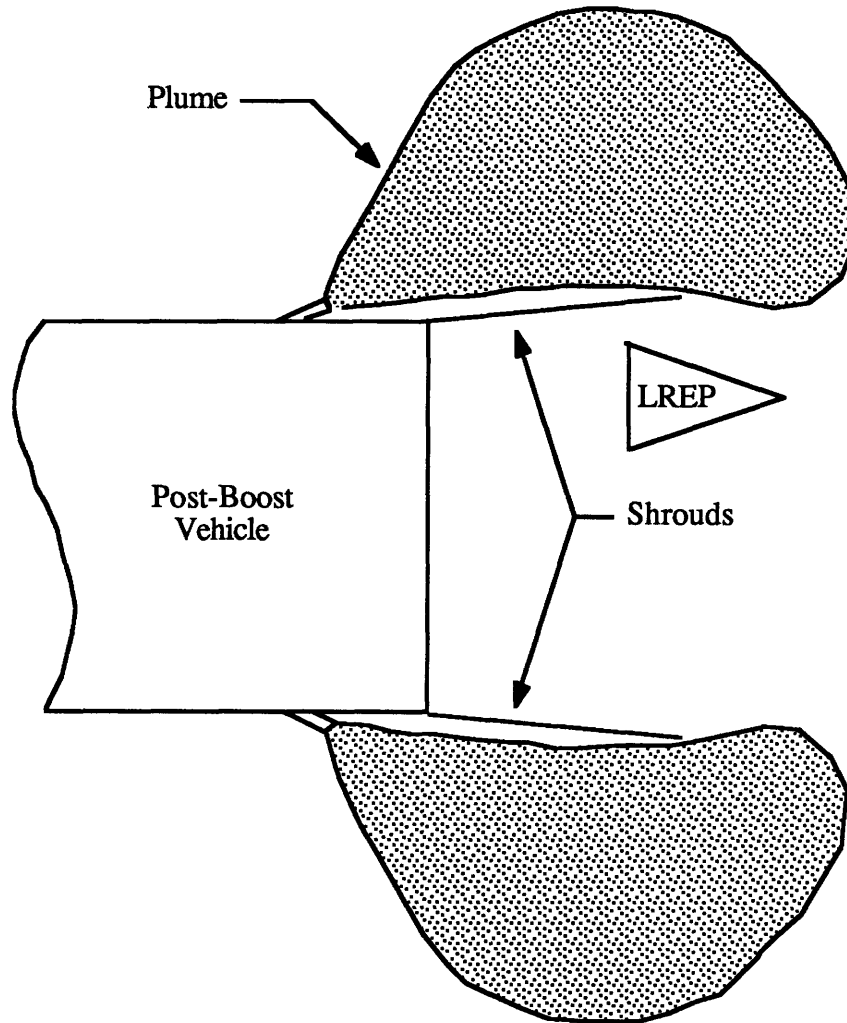
Figure 2.3.1: Plume Interaction.

The LREP has a spin angular momentum due to its spin rate, P, of 72 deg/sec.
Before the plume's interaction, an uncontrolled LREP has a precession rate, $\dot{\Psi}_c$, of
8 deg/sec and a coning angle, Θ_c, of 20 deg due to the ejection force [1]. This information
can be converted to an angular momentum by [2]

$$H_0 = I_v \, \dot{\Psi}_c \sin \Theta_c \,. \tag{2.3.4}$$

Substituting numbers yields $H_0 = 0.098$ kg m^2/sec. Figure 2.3.2 shows the spin
momentum and the ejector's induced momentum.
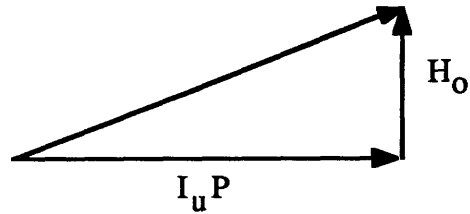
Figure 2.3.2: Angular Momentum Before Plume Interaction.

After the plume's interaction, an uncontrolled LREP has a precession rate of 10 deg/sec and a coning angle of 28 deg [1]. Using Equation 2.3.4 gives an angular momentum of $H_1 = 0.168$ kg m^2/sec. Therefore, the plume gives an increase in angular momentum, $\Delta H = 0.07$ kg m^2/sec. Figure 2.3.3 shows the plume's momentum contribution graphically.
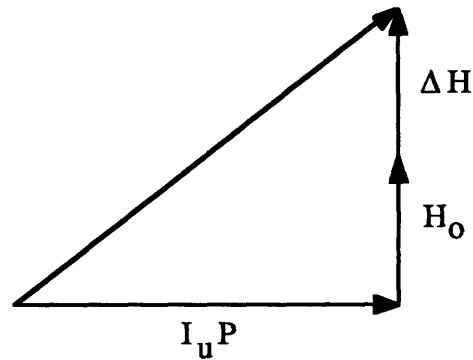
Figure 2.3.3: Angular Momentum After Plume Interaction.

The change in angular momentum caused by the plume's interaction is converted into an equivalent induced moment, for simulation purposes, by

$$M_{plume} = \frac{dH}{dt} .$$

(2.3.5)

The induced moment, unlike the induced forces, can be treated as an impulse. Assuming the induced angular momentum is constant over an interval $\Delta t = 0.01$ sec, then $M_{plume} = 7.0$ Nm. The performance requirements for the plume event are [1]:

plume event requirements: coning half-angle = 0 deg $\pm$ 3 deg

axial velocity = 2.5 m/s $\pm$ 0.2 m/s.

Chapter 3
Dynamic System Model

3.1 Coordinate Systems

Two natural coordinate systems come about from the dynamics of the LREP. One system is Earth-fixed and the other is body-fixed. In the Earth-fixed system, x is defined parallel to the Earth's surface and in the direction of the LREP's initial axial velocity, z is defined positive toward the earth's center, and y is defined such that x,y,z form a right triad. For the body-fixed system, u is defined as the spin axis of the LREP, and v and w are defined as initially parallel to y and z with origin at the LREP's center of mass. Thus, u,v,w also form a right triad. See Figure 3.1.1 below.
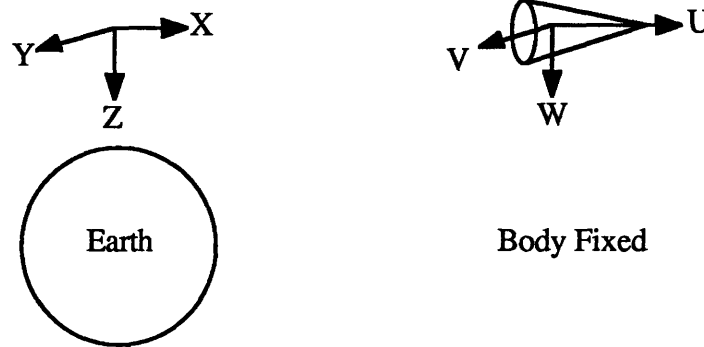
Figure 3.1.1: Earth-Fixed and Body-Fixed Coordinate Systems.

The performance specifications are given in the body-fixed system while the external forces, such as the plume forces and gravity, are in the Earth-fixed system. Therefore, conversion between coordinate systems is necessary. Three Euler angles, Φ, Θ, and Ψ, describe the orientation of the body system with respect to the Earth system. Φ is the rotation of x,y,z about y, which forms a new coordinate system x',y',z'. Θ is the rotation of x',y',z' about z', and thus forms a new coordinate system x'',y'',z''. Finally, Ψ is the rotation of x'',y'',z'' about x'', and forms a new system x''',y''',z'''. The body system u,v,w is defined as x''',y''',z''' and the rotations

are classified as a Type 1, 2-3-1 rotation sequence [3]. Figure 3.1.2 shows the angle rotations.
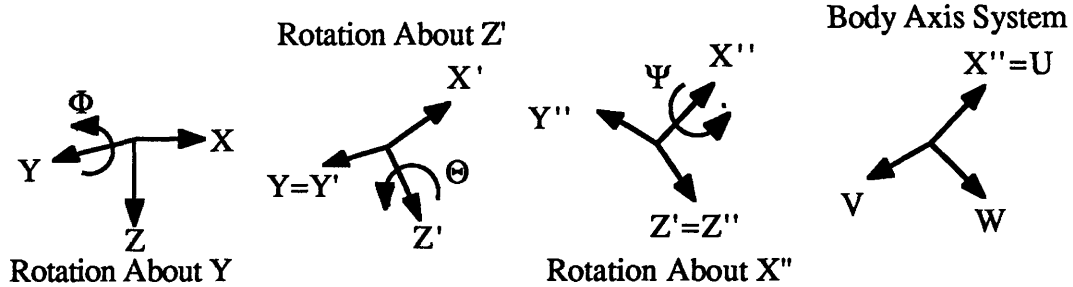
Figure 3.1.2: Euler Angle Rotations.

The direction cosine matrix, **A**, can be defined in terms of the appropriate sine and cosine functions of the Euler angles, and is used to convert a vector between systems. If x_b and x_e are vectors in the body and earth systems, respectively, then they are related by [4]

$$x_b = A\, x_e \tag{3.1.1}$$

$$x_e = A^T x_b \tag{3.1.2}$$

where **A** is defined as

$$A = \begin{bmatrix} ux & uy & uz \\ vx & vy & vz \\ wx & wy & wz \end{bmatrix}$$

and

$$ux = \cos(\Phi)\cos(\Theta) \tag{3.1.3a}$$

$$uy = \sin(\Theta) \tag{3.1.3b}$$

$$uz = -\sin(\Phi)\cos(\Theta) \tag{3.1.3c}$$

$$vx = -\cos(\Phi)\sin(\Theta)\cos(\Psi) + \sin(\Theta)\sin(\Psi) \tag{3.1.3d}$$

$$vy = \cos(\Theta)\cos(\Psi) \tag{3.1.3e}$$

$$vz = \sin(\Phi)\sin(\Theta)\cos(\Psi) + \cos(\Phi)\sin(\Psi) \tag{3.1.3f}$$

$$wx = \cos(\Phi)\sin(\Theta)\sin(\Psi) + \sin(\Phi)\cos(\Psi) \tag{3.1.3g}$$

$$wy = -\cos(\Theta)\sin(\Psi) \tag{3.1.3h}$$

$$wz = -\sin(\Phi)\sin(\Theta)\sin(\Psi) + \cos(\Phi)\cos(\Psi)\,. \tag{3.1.3i}$$

Because u,v,w are fixed with respect to the LREP, then Φ, Θ, and Ψ are functions of the LREP's rotation rate and the relationship is given by [3]

$$\frac{d\Phi}{dt} = Q\frac{\cos(\Psi)}{\cos(\Theta)} - R\frac{\sin(\Psi)}{\cos(\Theta)} \qquad (3.1.4)$$

$$\frac{d\Theta}{dt} = Q\sin(\Psi) + R\cos(\Psi) \qquad (3.1.5)$$

$$\frac{d\Psi}{dt} = P - Q\tan(\Theta)\cos(\Psi) + R\tan(\Theta)\sin(\Psi) \qquad (3.1.6)$$

where P,Q,R are the LREP's rotation rate about u,v,w, respectively.

3.2 Rotational Dynamics

The governing equation for the rotational dynamics of a rigid body is given by [5]

$$\Sigma M = \frac{dH}{dt} + \Omega \times H \qquad (3.2.1)$$

where M is the applied moment about u,v,w,

Ω is the rotation rate of the reference axis, and

H is the angular momentum of the LREP.

The angular momentum, H, about the LREP's center of mass, is given in body components as [6]

$$H_u = I_u P - I_{uv}Q - I_{uw}R \qquad (3.2.2a)$$

$$H_v = -I_{uv}P + I_v Q - I_{vw}R \qquad (3.2.2b)$$

$$H_w = -I_{uw}P - I_{vw}Q + I_w R . \qquad (3.2.2c)$$

Since the reference axis is fixed to the LREP, then $\Omega = Pu + Qv + Rw$ and the inertias are time invariant. Using these assumptions in Equation 3.2.1 yields

$$M_u = I_u\frac{dP}{dt} - I_{uv}\frac{dQ}{dt} - I_{uw}\frac{dR}{dt} + I_{vw}(R^2 - Q^2) + (I_w - I_v)QR + P(I_{uv}R - I_{uw}Q) \qquad (3.2.3a)$$

$$M_v = -I_{uv}\frac{dP}{dt} + I_v\frac{dQ}{dt} - I_{vw}\frac{dR}{dt} + I_{uw}(P^2 - R^2) + (I_u - I_w)PR + Q(I_{vw}P - I_{uv}R) \qquad (3.2.3b)$$

$$M_w = -I_{uw}\frac{dP}{dt} - I_{vw}\frac{dQ}{dt} + I_w\frac{dR}{dt} + I_{uv}(Q^2 - P^2) + (I_v - I_u)PQ + R(I_{uw}Q - I_{vw}P). \quad (3.2.3c)$$

However, the products of inertia are zero because the body system's origin is at the center of mass and the LREP is symmetric. Simplifying Equation 3.2.3 gives the rotational dynamic equations of motion for the LREP as

$$\frac{dP}{dt} = \frac{M_u}{I_u} \quad (3.2.4a)$$

$$\frac{dQ}{dt} = \frac{M_v}{I_v} - \frac{I_u - I_w}{I_v} PR \quad (3.2.4b)$$

$$\frac{dR}{dt} = \frac{M_w}{I_w} - \frac{I_v - I_u}{I_w} PQ. \quad (3.2.4c)$$

3.3 Translational Dynamics

The equation governing the translational motion of the body, assuming constant mass, is given by

$$\Sigma F = m\frac{dV}{dt} \quad (3.3.1)$$

where V is the LREP's velocity vector and is given by $V = Uu + Vv + Ww$. Taking the velocity's derivative yields

$$\frac{dV}{dt} = \frac{dU}{dt}u + \frac{dV}{dt}v + \frac{dW}{dt}w + U\frac{du}{dt} + V\frac{dv}{dt} + W\frac{dw}{dt} \quad (3.3.2)$$

and

$$\frac{du}{dt} = \Omega \times u \quad (3.3.3a)$$

$$\frac{dv}{dt} = \Omega \times v \quad (3.3.3b)$$

$$\frac{dw}{dt} = \Omega \times w . \quad (3.3.3c)$$

Substituting Equations 3.3.2 and 3.3.3 into 3.3.1 gives the governing translational dynamic equations of motion as

$$\frac{dU}{dt} = \frac{F_u}{m} - QW + RV \tag{3.3.4a}$$

$$\frac{dV}{dt} = \frac{F_v}{m} - RU + PW \tag{3.3.4b}$$

$$\frac{dW}{dt} = \frac{F_w}{m} - PV + QU . \tag{3.3.4c}$$

3.4 Coning Angle

The performance specifications are given in terms of the LREP's coning angle, Θ_c. It can be determined from the angular momentum along the three body axes, and is given by:

$$\cos \Theta_c = \frac{I_u P}{\sqrt{(I_u P)^2 + (I_v Q)^2 + (I_w R)^2}} . \tag{3.4.1}$$

P is the desired spin rate of 72 $^\circ$/sec. Thus the lateral rotation rates, Q and R, must be controlled in order to meet the coning angle specifications.

Chapter 4
Control System

4.1 System Overview

The control system presented consists of two accelerometers, four solenoid controlled valves, a state estimator, and electronic compensation. A block diagram of the system is shown in Figure 4.1.1. Control is achieved by activation of the solenoids and release of pressurized argon gas to produce the necessary control thrust. Two accelerometers are used as sensors. One accelerometer measures axial acceleration, $\dot{U}$, while the second accelerometer measures a linear combination of the LREP's rotation rate, Q, and the rotational acceleration $\dot{R}$. Hence, a state estimator is needed in order to reconstruct the accelerometers' outputs and give estimates of Q and R. Using these estimates along with U, the compensator makes decisions as to which thrusters must be activated.
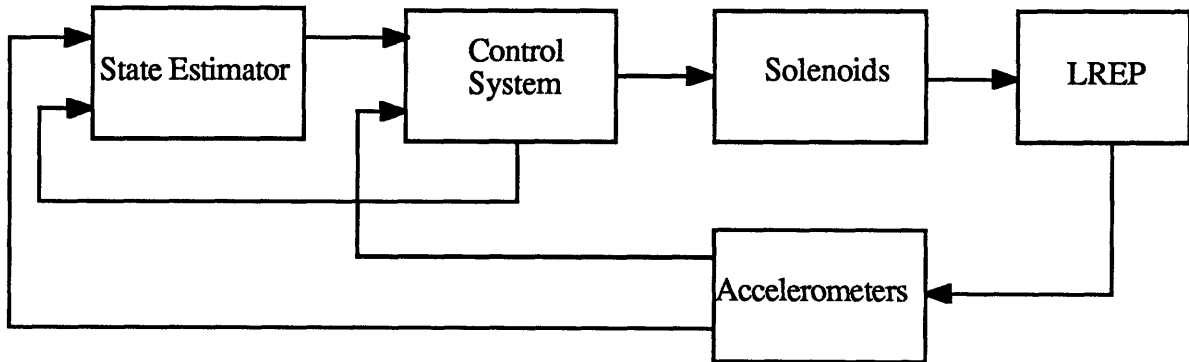
Figure 4.1.1: Control System Overview.

4.2 Sensor Configuration

The variables of interest are Q, R, and U, because the goal is to minimize the coning angle and axial velocity deviations. Accelerometers measure inertial accelerations and output them in the body coordinate system. All corriolis forces are zero because the

accelerometers are rigidly attached to the LREP, and the measurement equations are derived

from the general acceleration equation [7]

$$a = a_{cm} + \frac{d\Omega}{dt} \times r + \Omega \times (\Omega \times r).$$ (4.2.1)

The acceleration of the LREP's center of mass, a_{cm}, is expressed as

$$a_{cm} = \frac{dU}{dt} u + \frac{dV}{dt} v + \frac{dW}{dt} w.$$ (4.2.2)

The rotation rate of the LREP about it's center of mass, Ω, is given by

$$\Omega = P u + Q v + R w$$ (4.2.3)

and the location of the accelerometer, r, is

$$r = r_u u + r_v v + r_w w.$$ (4.2.4)

The accelerometer output equations, found by substituting a_{cg}, Ω, and r into Equation

4.2.1, are

$$a_u = \frac{dU}{dt} - (Q^2 + R^2)r_u + (PQ - \frac{dR}{dt})r_v + (PR + \frac{dQ}{dt})r_w$$ (4.2.5a)

$$a_v = \frac{dV}{dt} + (PQ + \frac{dR}{dt})r_u - (P^2 + R^2)r_v + (QR)r_w$$ (4.2.5b)

$$a_w = \frac{dW}{dt} + (PR - \frac{dQ}{dt})r_u + (QR)r_v - (P^2 + Q^2)r_w$$ (4.2.5b)

where a_u, a_v, or a_w is the measurement for an accelerometer's sensitive axis aligned with u,

v, or w respectively.

One accelerometer is located at $r_1 = 0$ and a second accelerometer is located at

$r_2 = r_v v$ because Q, R, and U must be measured. Figure 4.2.1 shows the location of the

accelerometers. This configuration requires that both accelerometers are mounted in a plane

orthogonal to u, with the first accelerometer located at the center of mass. The

accelerometer outputs in terms of the variables of interest are

$$a_1 = \frac{dU}{dt}$$ (4.2.6)

$$a_2 = \frac{dU}{dt} + (PQ - \frac{dR}{dt})r_v.$$ (4.2.7)

The measurements for axial velocity and coning angle control are expressed in terms of the two accelerometer outputs as

$$y_{attitude} = PQ - \frac{dR}{dt} = \frac{1}{r_v}(a_2 - a_1) \qquad (4.2.8)$$

$$y_{axial} = U = \int a_1 \, dt \ . \qquad (4.2.9)$$

W

Accelerometer 1 —————————————— Accelerometer 2

V

Upper Plate : Top View

U

Upper Plate ——

V

Base Plate ——

LREP : Side View
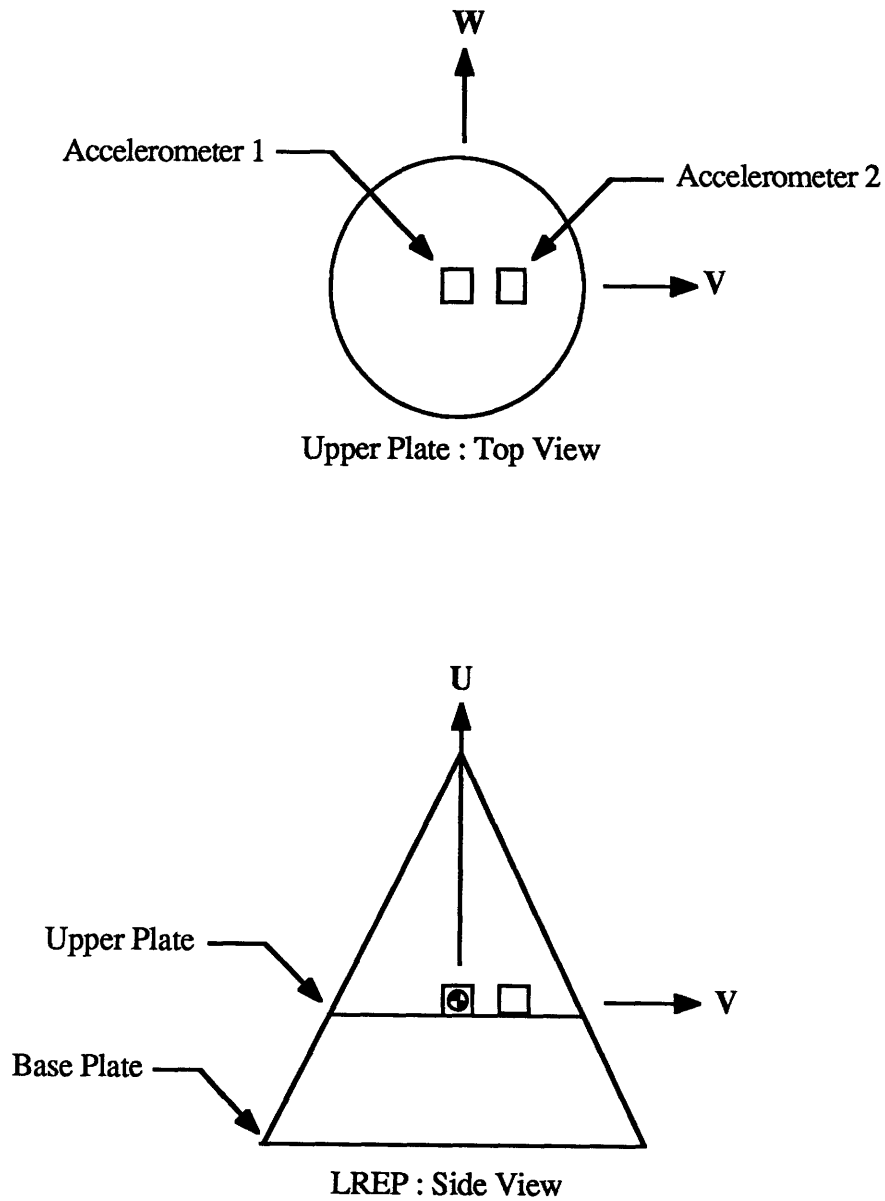
Figure 4.2.1: Accelerometer Mounting Configuration.

4.3 Actuator System

The actuator system consists of an Argon tank, pressure regulator, and four solenoid valves. See Figure 4.3.1. Argon is chosen because it is inert, storable, and safe to handle. Control forces are obtained by energizing a solenoid valve and releasing pressurized Argon when thrust is needed. A pressure regulator is used to supply constant pressure to the solenoids.
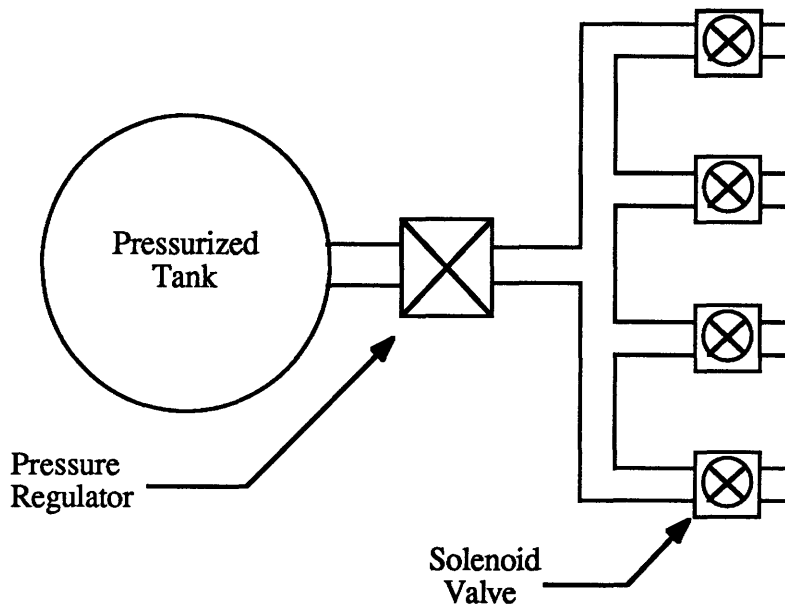
Figure 4.3.1: Actuator System.

The propellant mass needed is given by

$$m_{prop} = \frac{1.0}{g \cdot I_{sp}} \int [F_1(t) + F_2(t) + F_3(t) + F_4(t)] \, dt \qquad (4.3.1)$$

where F_1, F_2, F_3, F_4 are the thrusts delivered by each valve,

I_{sp} is the specific impulse of Argon, and

g is the gravitational constant.

Since solenoid valves are binary devices, the control thrust can be expressed as

$$F_i = \begin{cases} 0 & \text{valve closed} \\ 1.5 \text{ N} & \text{valve open} \end{cases} \cdot$$

The theoretical specific impulse of a gas is [8]

$$I_{sp} = \frac{1}{g} \sqrt{\frac{2R_0 T}{M_0} \frac{\gamma}{(\gamma-1)}} \qquad (4.3.2)$$

where γ = specific heat ratio,

T = temperature of the gas ($^\circ$K),

M_0 = molecular weight of the gas, and

R_0 = ideal gas constant.

Assuming that the Argon temperature at deployment, T_d, is 243 $^\circ$K [9], the specific impulse is 51 seconds. The maximum amount of Argon needed for this system, determined from computer simulations, is 4.0 grams.

4.3.1 Pressurized Tank

The size of the pressurized tank is important in determining if mass and volume specifications can be achieved. The orifice diameter, d, for the chosen solenoid valves is 2.5 mm [10] and the control thrust level, | F |, is 1.5 N. This dictates a regulator secondary pressure, P_s, of

$$P_s = \frac{4 \; | \; F \; |}{\pi \; d^2} = 0.3 \text{ MPa} \,. \qquad (4.3.1.1)$$

The following boundary conditions must be met in order to choose the primary pressure, P_p:

a) after disturbances are removed $P_p \geq P_s$ and $m = \Delta m \geq 0$

b) on the ground before launch $T_g = 293 \; ^\circ$K and $m = m_0 + \Delta m$

where m_0 = Argon mass needed for control (including a safety factor of 2.5) = 10 grams,

Δm = residual Argon mass, and

T_g = temperature of the Argon on the ground.

The ideal gas law gives the governing equations for the tank volume, V_t, as

$$P_s V_t = \Delta m \, R_o \, T_d \qquad (4.3.1.2a)$$

$$P_g V_t = (\Delta m + m_o) \, R_o \, T_g \qquad (4.3.1.2b)$$

where P_g is the pressure of the tank on the ground.

Combining Equations 4.3.1.2a and 4.3.1.2b gives

$$P_g = (\frac{1}{\rho} + 1) \frac{T_g}{T_d} P_s \qquad (4.3.1.3a)$$

$$m = (1 + \rho) \, m_o \qquad (4.3.1.3b)$$

$$V_t = \rho \, (\frac{m_o \, R \, T_d}{P_s}) \qquad (4.3.1.3c)$$

where $\rho = \dfrac{\Delta m}{m_o}$.

The goal is to choose ρ such that P_g, m, and V_t are minimized, but it is apparent from Equation 4.3.1.3 that this cannot be accomplished. Thus a cost function, J, which weights each of the three parameters is used and the optimal mass ratio, ρ_{opt}, is chosen such that J is minimized. The cost function is

$$J = 0.2 \, \frac{m}{m_{max}} + 0.2 \, \frac{V_t}{V_{t\,max}} + 0.6 \, \frac{P_g}{P_{g\,max}} \qquad (4.3.1.4)$$

and the optimal mass ratio is restricted between 0.1 and 1.0 because of the excessive values of m and P_g beyond this range. P_g is weighted more heavily because of the structural stresses caused by large internal pressures. Substitution of each parameter and the corresponding maximum value gives the cost function, J, in terms of the mass ratio as

$$J = 0.155 + 0.3 \, \rho + \frac{0.055}{\rho}. \qquad (4.3.1.5)$$

The optimal ρ, found by setting $\dfrac{dJ}{d\rho} = 0$ and solving for ρ, is

$$\rho_{opt} = 0.426$$

and the optimal parameters are

$$V_t = 7.2*10^{-4}\,m^3$$

$$P_g = 1.21\,MPa$$

$$m = 14.3\,grams.$$

Figure 4.3.1.1 shows the optimal mass ratio.
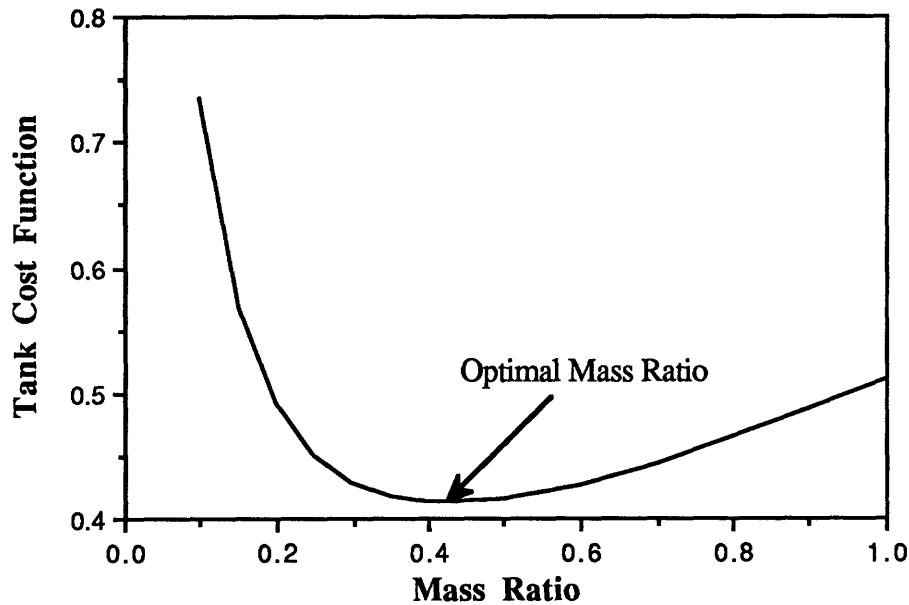
Figure 4.3.1.1: Tank Cost Function vs Mass Ratio.

4.3.2 Solenoid Configuration

The solenoids are mounted in the base plate of the LREP because it is made of a rigid material which will not deform under loading. Three solenoids are mounted on the outer perimeter of the base plate, and positioned 120° apart with their nozzles angled 60° from the LREP's bottom. The fourth is positioned directly in the center with its nozzle pointing in the -u direction. Figure 4.3.2.1 shows the mounting configuration.

The three outer valve nozzles are angled at 60° in order to achieve full controllability of U, Q, and R with the minimum number of valves. This allows simultaneous control of axial velocity and coning angle. Figure 4.3.2.2 shows that the 60° thruster angle is optimal

W

−30° F₃

F₁ →

V

Top View

60°

F₂

U

F_1, F_2, F_3 are angled at
60° from the LREP's bottom

F₁

60°

V

F₂

F₄

LREP : Side View
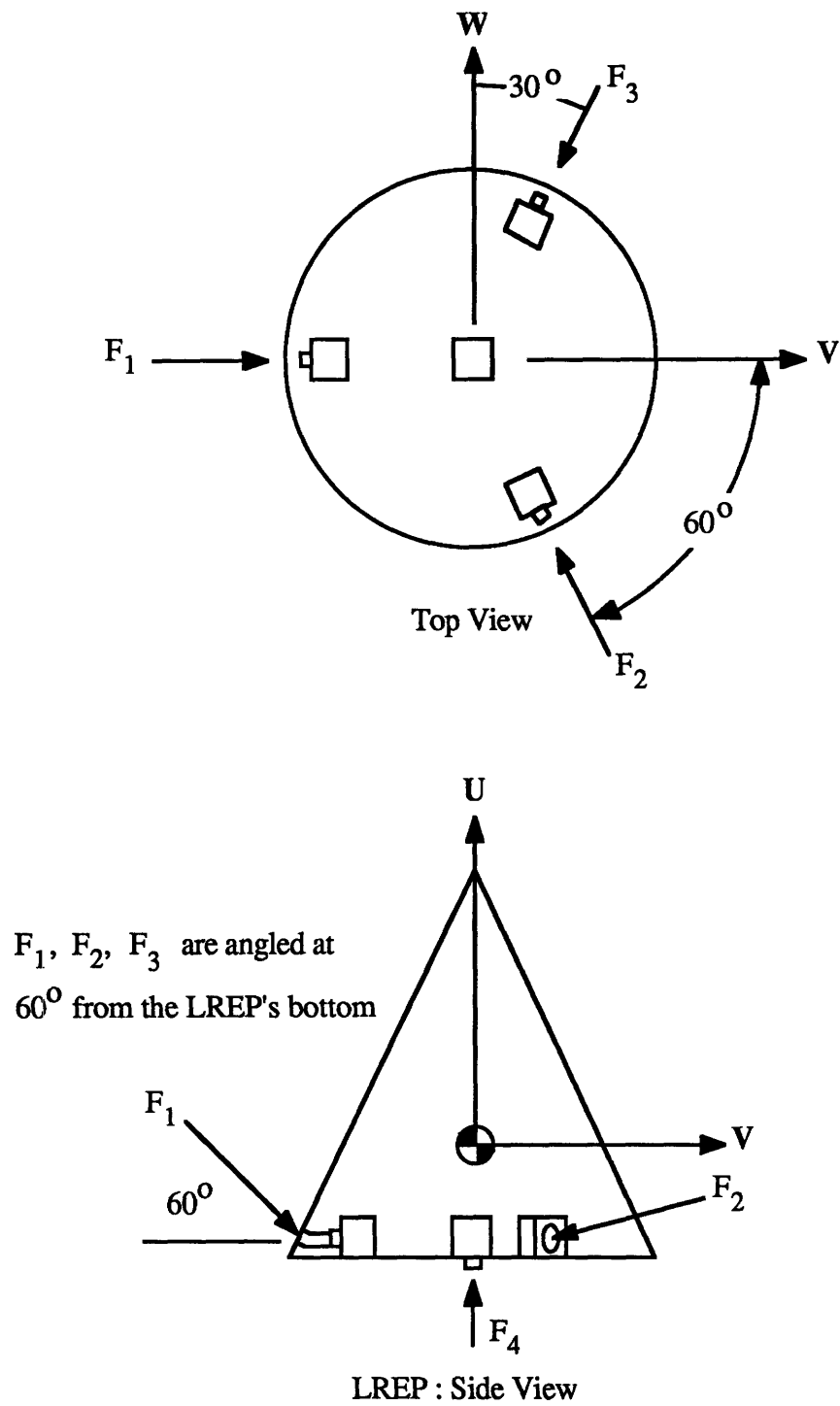
Figure 4.3.2.1: Solenoid Mounting Configuration.

for minimizing the propellant mass. The effective moment arm, r_{eff}, for the outer solenoid

valves is given by

$$r_{eff} = r_1\cos\mu + r_2\sin\mu \qquad (4.3.2.1)$$

where r_1 = orthogonal distance from the center of mass to the base plate, and

r_2 = base plate radius.

Therefore, the effective moment arm is 0.78 meters.
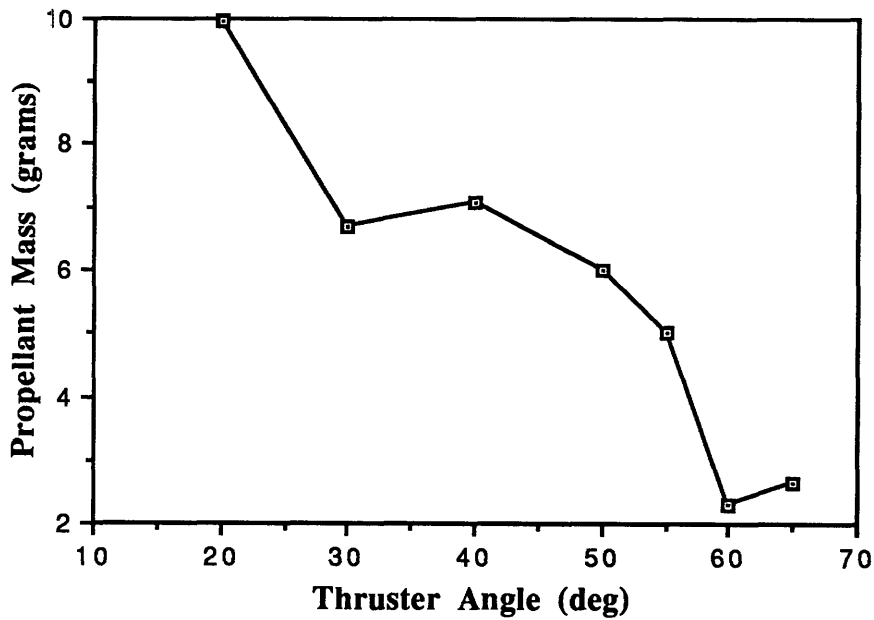
Figure 4.3.2.2: Propellant Mass vs Thruster Angle.

4.4 Modified Dynamic System Model

The governing equations of motion are modified in order to include the solenoid configuration. The net forces on the LREP, in terms of the individual solenoid forces, are

$$F_u = - (F_1 + F_2 + F_3)\sin\mu + F_4 \qquad (4.4.1a)$$

$$F_v = \{F_1 - (F_2 + F_3)\sin30^\circ\}\cos\mu \qquad (4.4.1b)$$

$$F_w = (F_2 - F_3)\cos30^\circ \cos\mu \qquad (4.4.1c)$$

where μ is the nozzle angle of 60°. The net moments, in terms of the individual solenoid forces, are

$$M_u = 0 \qquad (4.4.2a)$$

$$M_v = (F_2 - F_3)\cos30^\circ r_{eff} \qquad (4.4.2b)$$

$$M_w = \{- F_1 + (F_2 + F_3)\sin30^\circ\}r_{eff} . \qquad (4.4.2c)$$

A new variable, L, is introduced in order to normalize the solenoid forces and is defined by

$$L_i = \frac{F_i}{|F|} \qquad \forall \; i = 1,2,3,4 \quad \text{such that } L_i = \left\{ \begin{array}{l} 0 \;\; \text{if solenoid is off} \\ 1 \;\; \text{if solenoid is on} \end{array} \right.$$

where $|F|$ is the thrust level of 1.5 N. Using the normalized variable in Equation 4.4.2, and combining with Equation 3.2.3 gives

$$\frac{dP}{dt} = 0 \qquad (4.4.3a)$$

$$\frac{dQ}{dt} = (1 - \frac{I_u}{I_v})P R + \frac{|F| \, r_{eff} \cos30^\circ}{I_v} (L_2 - L_3) \qquad (4.4.3b)$$

$$\frac{dR}{dt} = - (1 - \frac{I_u}{I_v})P Q - \frac{|F| \, r_{eff}}{I_v} [L_1 - \sin30^\circ (L_2 + L_3)] \qquad (4.4.3c)$$

and substituting numbers yields the modified rotational dynamics

$$\frac{dQ}{dt} = 1.1\,R + 0.5(L_2 - L_3) \qquad (4.4.4a)$$

$$\frac{dR}{dt} = -1.1\,Q - 0.6L_1 + 0.3(L_2 + L_3) \,. \qquad (4.4.4b)$$

The modified translational dynamics are found by substituting the normalized variable in Equation 4.4.1, and combining with Equation 3.3.4 to give

$$\frac{dU}{dt} = -\,QW + RV - 0.43(L_1 + L_2 + L_3) + 0.5\,L_4 \qquad (4.4.5a)$$

$$\frac{dV}{dt} = PW - RU + 0.25\,L_1 - 0.13(L_2 + L_3) \qquad (4.4.5b)$$

$$\frac{dW}{dt} = QU - PV + 0.22(L_2 - L_3) \,. \qquad (4.4.5c)$$

Equations 4.4.3 and 4.4.4 are the dynamic equations used for control law design. The only assumptions are zero products of inertia and zero resultant moment about u.

4.5 State Estimator

A state estimator is needed to convert the attitude measurement, $y_{attitude}$, into estimates for Q and R. From Equation 4.2.8 , the measurement is

$$y_{attitude} = PQ - \frac{dR}{dt} = \frac{1}{r_v}(a_2 - a_1) \,. \qquad (4.2.8)$$

The LREP's attitude dynamics are given by Equation 4.4.4 as

$$\frac{dQ}{dt} = 1.1\,R + 0.5\,(L_2 - L_3) \qquad (4.4.4a)$$

$$\frac{dR}{dt} = -1.1\,Q - 0.6\,L_1 + 0.3\,(L_2 + L_3) \,. \qquad (4.4.4b)$$

Combining Equation 4.4.3b with the measurement gives

$$y_{attitude} = PQ - \frac{dR}{dt} = 2.36Q + 0.6 L_1 - 0.3 (L_2 + L_3) . \qquad (4.5.1)$$

Define the state vector, x, and the control input, u (Note: x and u are not the unit vectors) as

$$x = \begin{bmatrix} Q \\ R \end{bmatrix} \qquad u = \begin{bmatrix} L_1 \\ L_2 \\ L_3 \end{bmatrix} .$$

The LREP's attitude dynamics are given by

$$\dot{x} = A x + B u \qquad (4.5.2a)$$

and the measurement as

$$y = C x + D u \qquad (4.5.2b)$$

where

$$A = \begin{bmatrix} 0 & 1.1 \\ -1.1 & 0 \end{bmatrix} \qquad B = \begin{bmatrix} 0 & .5 & -.5 \\ -.6 & .3 & .3 \end{bmatrix}$$

$$C = [2.36 \ 0] \qquad D = [.6 \ -.3 \ .3] .$$

The purpose of the state estimator is to reconstruct the rotation rates, Q and R, from the measurement, y. The estimator structure is given by [11]

$$\dot{\hat{x}} = A \hat{x} + B u + H (y - \hat{y}) \qquad (4.5.3a)$$

$$\hat{y} = C \hat{x} + D u \qquad (4.5.3b)$$

where $\hat{x}$ is the state estimate of x,

$\hat{y}$ is the estimated measurement, and

H is a gain matrix which determines how the estimation error affects the estimator. The state estimator block diagram is shown in Figure 4.5.1.
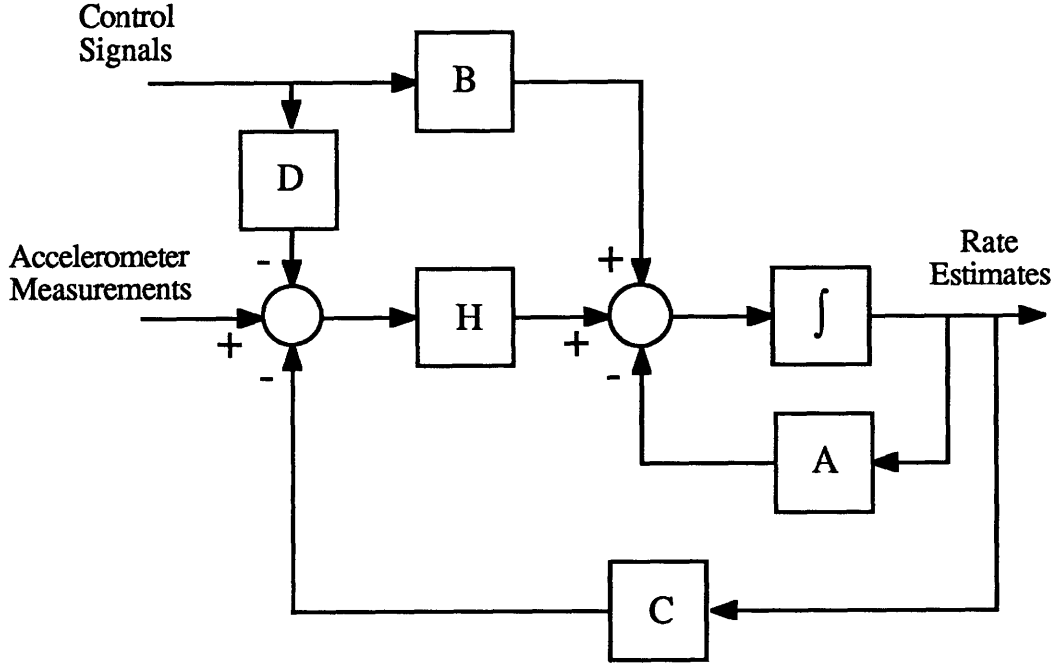
Figure 4.5.1: State Estimator Block Diagram.

The LREP and estimator states are combined to give

$$\begin{bmatrix} \dot{x} \\ \dot{\hat{x}} \end{bmatrix} = \begin{bmatrix} A & 0 \\ HC & A\text{-}HC \end{bmatrix} \begin{bmatrix} x \\ \hat{x} \end{bmatrix} + \begin{bmatrix} B \\ B \end{bmatrix} u . \qquad (4.5.4)$$

The estimator dynamics are coupled with the LREP dynamics by the gain matrix, H. The estimation error state, $\tilde{x}$, is defined by

$$\tilde{x} = x - \hat{x} \qquad (4.5.5)$$

and the estimation error dynamics are given by

$$\dot{\tilde{x}} = (A\text{-}HC)\ \tilde{x} . \qquad (4.5.6)$$

Therefore, the estimator gain matrix, H, must satisfy

$$Re\ \{\ \lambda\ (A\text{-}HC)\} \leq 0 \qquad (4.5.7)$$

for a stable estimation of Q and R. The solution for a constant gain matrix, H, is given by [12]

$$H = S\ C^T\ V_2^{-1} \qquad (4.5.8)$$

where S is the solution to the algebraic observer Riccati equation

$$0 = A S + S A^T + V_1 - S C^T V_2^{-1} C S .$$ (4.5.9)

This estimator gives the minimum mean square linear estimate of x [13] for a system driven by white process noise of intensity

$$V_1 = G V_3 G^T \qquad V_3 > 0$$ (4.5.10a)

and with white measurement noise intensity

$$V_2 > 0 .$$ (4.5.10b)

Therefore, H minimizes the cost function [14]

$$J = \text{trace}[E \{ \tilde{x}(t) \tilde{x}^T(t) \}]$$

where E is the expectation operator. The noise matrices chosen for the LREP system are

$$G^T = [1 \ 1] \qquad V_3 = 1 \qquad V_2 = 4.4 * 10^{-5}$$

and the optimal gain matrix is

$$H = [151.2 \ 150.2]^T .$$

The state estimation error matrix, A - HC, is

$$A - HC = \begin{bmatrix} -356.4 & 1.1 \\ -355.1 & 0 \end{bmatrix}$$

and the eigenvalues and corresponding eigenvectors are

$$\lambda_1 = -1.1 \text{ rad/sec} \qquad \lambda_2 = -355.3 \text{ rad/sec}$$

$$\upsilon_1 = \begin{bmatrix} .0031 \\ 1 \end{bmatrix} \qquad \upsilon_2 = \begin{bmatrix} .707 \\ .707 \end{bmatrix} .$$

It is clear from examination of the eigenvectors that estimation of Q is dominated by λ_2 while estimation of R is dominated by λ_1. This result is consistent with the measurement since y is a linear combination of Q and $\dot{R}$.

This estimator provides an optimal compromise between estimator bandwidth and sensor noise immunity [15]. The noise-bandwidth tradeoff is best shown by a root locus

of the state estimation error poles as the sensor noise varies. Using the same G and V_3 as given above, the sensor noise intensity is varied by

$$0.01 \leq V_2 \leq 10 .$$

The root locus is shown in Figure 4.5.2. As the sensor noise increases, the estimation error poles approach s = ± 1.1j rad/sec which are the open loop eigenvalues of the LREP system. Thus, the estimator approaches open loop estimation because the sensor measurement becomes excessively corrupted by noise. As the sensor noise intensity decreases, the bandwidth of the estimator increases as is evident from one pole moving toward -∞. However, the second pole moves toward a fictitious zero at s = -1.1 rad/sec. The result arises from the fact that the poles of the estimation error dynamics approach the zeros of

$$H(s) = C (sI - A)^{-1}G \qquad (4.5.11)$$

as the sensor noise approaches zero[16]. For the LREP's estimator, H(s) has a zero at s = -1.1 rad/sec as verified by Figure 4.5.2.
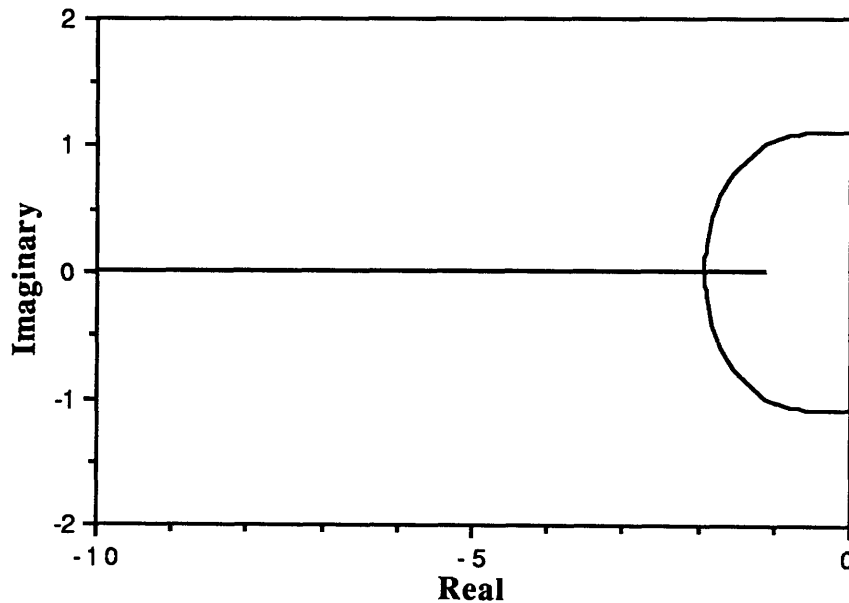

Figure 4.5.2: Estimation Error Root Locus.

4.6 Control Laws

The control laws are presented in two sections: attitude control and axial velocity control. Equations 4.4.4 and 4.4.5 show that the rotational dynamics are independent of the translational, but the converse is not true. Therefore axial velocity control is dependent on attitude control. The control laws are bang-bang with a dead band because of the switching nature of solenoid valves.

4.6.1 Attitude Control

The attitude control law is derived by considering the performance criteria along with the degrees of freedom established by the actuator configuration. The coning angle is given in Equation 3.4.1 as

$$\cos \Theta_c = \frac{I_u P}{\sqrt{(I_u P)^2 + (I_v Q)^2 + (I_w R)^2}}. \qquad (3.4.1)$$

Since P is constant, the above equation can be rewritten in terms of the control variables, Q and R, as

$$\sqrt{Q^2 + R^2} = \frac{I_u}{I_v} P \tan(\Theta_c). \qquad (4.6.1.1)$$

Substituting numbers and using the 3° coning angle performance criteria gives

$$\sqrt{Q^2 + R^2} = 0.008. \qquad (4.6.1.2)$$

The coning angle performance criteria is expressed by the equation of a circle of radius 0.008 rad/sec and is depicted graphically in Figure 4.6.1.1.

An acceptable control law is one which maps any initial conditions of the attitude states into a trajectory which ends inside the performance region. The performance region is defined as
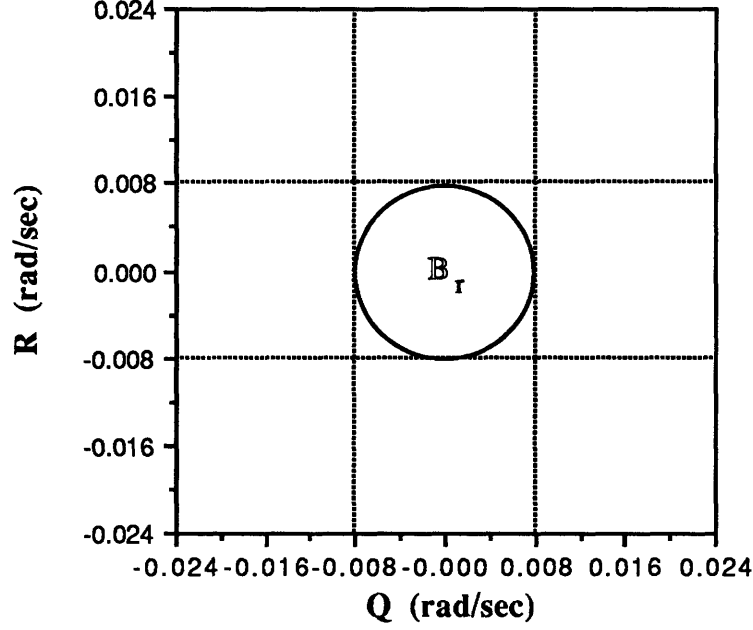
Figure 4.6.1.1: Attitude Control System's Performance Region.

$$\mathbb{B}_{0.008} = \{x : \| x \|_2 \leq 0.008 , x \in \mathfrak{R}^2 \} \qquad (4.6.1.3)$$

where $x = [Q\ R]^T$ and the set of all acceptable control laws, $\mathbb{L}$, are given by

$$\mathbb{L} : x(0) \rightarrow x(\infty) \qquad \text{where } x(0) \in \mathfrak{R}^2 \text{ and } x(\infty) \in \mathbb{B}_{0.008} . \qquad (4.6.1.4)$$

The attitude control law chosen is given by

$$L_1 = R_{pos} + (Q_{pos} \bullet R_{off}) \qquad (4.6.1.5a)$$

$$L_2 = Q_{neg} \qquad (4.6.1.5b)$$

$$L_3 = R_{neg} + (Q_{pos} \bullet R_{off}) \qquad (4.6.1.5c)$$

where + and • denote the logical operators OR and AND, respectively. The logical variables R_{pos}, R_{neg}, Q_{pos}, Q_{neg}, and R_{off} are defined by

$$R_{pos} = \begin{cases} \text{true} & R > \text{dead band} \\ \text{false} & \text{otherwise} \end{cases} \qquad (4.6.1.6a)$$

$$R_{neg} = \begin{cases} \text{true} & R < \text{- dead band} \\ \text{false} & \text{otherwise} \end{cases} \qquad (4.6.1.6b)$$

$$Q_{pos} = \begin{cases} \text{true} & Q > \text{dead band} \\ \text{false} & \text{otherwise} \end{cases} \qquad (4.6.1.6c)$$

$$Q_{neg} = \begin{cases} \text{true} & Q < \text{- dead band} \\ \text{false} & \text{otherwise} \end{cases} \qquad (4.6.1.6d)$$

$$R_{off} = \begin{cases} \text{true} & |R| < \text{dead band} \\ \text{false} & \text{otherwise} \end{cases} \cdot \qquad (4.6.1.6e)$$

Dead band is chosen to meet performance specifications and is discussed in greater detail at the end of this section.

A physical interpretation of the control law can be established by state trajectory analysis. Since there are three solenoids, each on or off, there are 2^3 possible operating regimes which may occur. These regimes, along with the corresponding dynamic equations of motion, are

I) $L_1 = L_2 = L_3 = 0$ $\dfrac{dQ}{dt} = 1.1\,R$ $\dfrac{dR}{dt} = -1.1\,Q$

II) $L_1 = 1, L_2 = L_3 = 0$ $\dfrac{dQ}{dt} = 1.1\,R$ $\dfrac{dR}{dt} = -1.1\,Q - 0.6$

III) $L_1 = 0, L_2 = L_3 = 1$ $\dfrac{dQ}{dt} = 1.1\,R$ $\dfrac{dR}{dt} = -1.1\,Q + 0.6$

IV) $L_1 = L_2 = 1, L_3 = 0$ $\dfrac{dQ}{dt} = 1.1\,R + 0.5$ $\dfrac{dR}{dt} = -1.1\,Q - 0.3$

V) $L_1 = L_3 = 1, L_2 = 0$ $\dfrac{dQ}{dt} = 1.1\,R - 0.5$ $\dfrac{dR}{dt} = -1.1\,Q - 0.3$

VI) $L_2 = 1, L_1 = L_3 = 0$ $\dfrac{dQ}{dt} = 1.1\,R + 0.5$ $\dfrac{dR}{dt} = -1.1\,Q + 0.3$

VII) $L_3 = 1, L_1 = L_2 = 0$ $\dfrac{dQ}{dt} = 1.1\,R - 0.5$ $\dfrac{dR}{dt} = -1.1\,Q + 0.3$.

The eighth region of operation corresponds to all solenoids on and is equivalent to region I (i.e., all solenoids off). Assuming that Q,R << 0.3 rad/sec, the state trajectories can be sketched for each region of operation. Figure 4.6.1.2 shows the trajectories where each region of operation is valid. It can be seen from this figure that the control law results in the terminal states inside the performance circle.
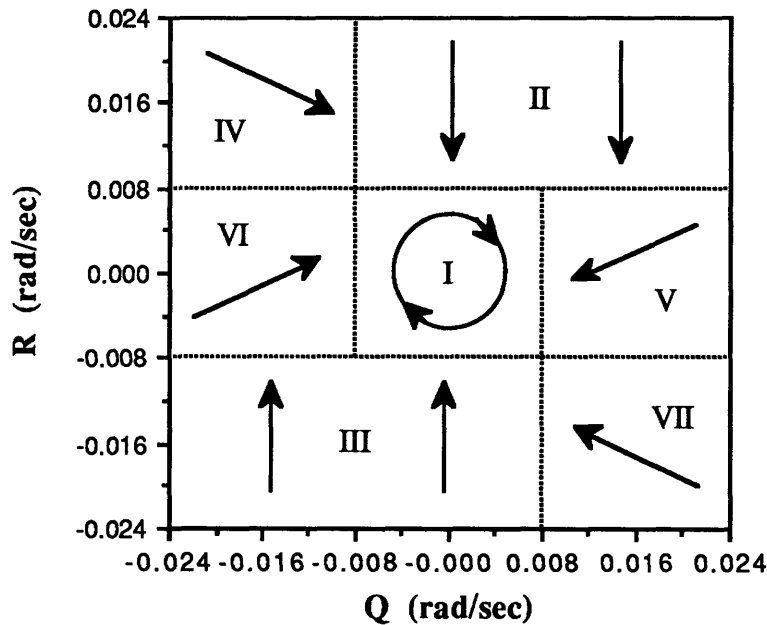
Figure 4.6.1.2: State Trajectories for the Attitude Control System.

Lyapunov Stability Theory is utilized to prove the control law ∈ L. Choosing the continuous positive definite function, V, as

$$V = \frac{1}{2}(Q^2 + R^2) \qquad (4.6.1.7)$$

Setting the dynamic equations for each region of operation into the form

$$\frac{dQ}{dt} = 1.1 R + a \qquad \frac{dR}{dt} = -1.1 Q + b$$

gives

$$\dot{V}(t,Q,R) = a Q + b R . \qquad (4.6.1.8)$$

Comparison of a and b for each region of operation shows that

$$\dot{V}(t,Q,R) < 0 \quad \text{for} \quad \sqrt{Q^2 + R^2} > \text{dead band}$$

and

$$\dot{V}(t,Q,R) = 0 \quad \text{for} \quad \sqrt{Q^2 + R^2} \leq \text{dead band}$$

and proves   a) global asymptotic stability [17] of the attitude control system as

$$\text{dead band} \rightarrow 0$$

and

b) the control law $\in$ L for dead band ≤ 0.008 rad/sec.

The dead band is chosen as 0.006 rad/sec because it meets the performance specifications. As the dead band is reduced below this level, the required propellant mass increases. At the same time, it should not be any larger than 0.006 rad/sec because variations in the spin rate or inertias could result in a coning angle larger than 3°.

4.6.2 Axial Velocity Control

The modified translational dynamics given by Equation 4.4.5, combined with the gravity contribution yields

$$\frac{dU}{dt} = -QW + RV - .43(L_1 + L_2 + L_3) + .5 L_4 - g [\sin(\Phi)\cos(\Theta)] \qquad (4.6.2.1a)$$

$$\frac{dV}{dt} = PW - RU + .25L_1 - .13(L_2 + L_3) + g[\sin(\Phi)\sin(\Theta)\cos(\Psi) + \cos(\Phi)\sin(\Psi)] \quad (4.6.2.1b)$$

$$\frac{dW}{dt} = QU - PV + .22(L_2 - L_3) - g [\sin(\Phi)\sin(\Theta)\sin(\Psi) + \cos(\Phi)\cos(\Psi)] . \qquad (4.6.2.1c)$$

Initial conditions on the Euler Angles, Φ, Θ, and Ψ, are

$$\Phi\,(0) = 0$$

$$\Theta\,(0) = 0$$

$$\Psi\,(0) = \Psi_o\,.$$

The attitude control law guarantees that Q,R « 1 and, more specifically, $\sqrt{Q^2 + R^2} \le 0.008$ rad/sec in steady-state. Assuming the attitude control system performs as designed, the Euler angle derivatives given by Equations 3.1.4, 3.1.5, and 3.1.6 can be approximated as

$$\frac{d\Phi}{dt} \approx 0$$

$$\frac{d\Theta}{dt} \approx 0$$

$$\frac{d\Psi}{dt} \approx P = 72\ ^o/sec\,.$$

Combining with the initial conditions yields

$$\Phi\,(t)\ « 1$$

$$\Theta\,(t)\ « 1$$

$$\Psi\,(t)\ \approx \Psi_o + Pt\,.$$

Equation 4.6.2.1a is simplified, using these approximations, to

$$\frac{dU}{dt} \approx -0.43(L_1 + L_2 + L_3) + 0.5\,L_4\,. \qquad (4.6.2.2)$$

The axial velocity error, $\tilde{u}$, is defined as

$$\tilde{u} = 2.5 - U\,.$$

The performance criterion is expressed in terms of $\tilde{u}$ as

$$|\,\tilde{u}\,| \le 0.2\ m/sec$$

and the set of all acceptable axial velocity control laws, M, is given by

$$M : \tilde{u}\,(0) \rightarrow \tilde{u}\,(\infty) \qquad \text{where } \tilde{u}\,(0) \in \Re, \ \tilde{u}\,(\infty) \in \mathbb{B}_{0.2} \qquad (4.6.2.3)$$

where

$$\mathbb{B}_{0.2} = \{ \ \tilde{u} : |\tilde{u}| \leq 0.2, \tilde{u} \in \Re \ \}. \qquad (4.6.2.4)$$

The axial velocity control law is given by

$$L_1 = \tilde{u}_{neg} \qquad (4.6.2.5a)$$

$$L_2 = \tilde{u}_{neg} \qquad (4.6.2.5b)$$

$$L_3 = \tilde{u}_{neg} \qquad (4.6.2.5c)$$

$$L_4 = \tilde{u}_{pos} \qquad (4.6.2.5d)$$

where $\tilde{u}_{pos}$ and $\tilde{u}_{neg}$ are defined by

$$\tilde{u}_{pos} = \begin{cases} \text{true} & \tilde{u} > \text{dead band} \\ \text{false} & \text{otherwise} \end{cases} \qquad (4.6.2.6a)$$

$$\tilde{u}_{neg} = \begin{cases} \text{true} & \tilde{u} < -\text{dead band} \\ \text{false} & \text{otherwise} \end{cases} \cdot \qquad (4.6.2.6b)$$

Dead band is chosen to meet performance specifications and is discussed in greater detail at the end of this section. Figure 4.6.2.1 shows a block diagram of the axial velocity controller.
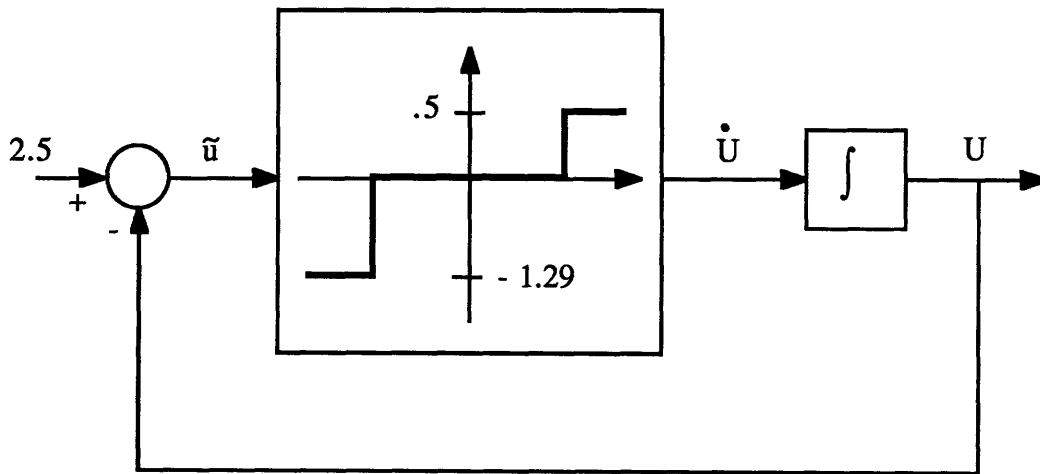

Figure 4.6.2.1: Block Diagram of the Axial Velocity Control System.

Lyapunov Stability Theory is again utilized to prove the control law $\in$ M. Choose the continuous, positive definite function, V, as

$$V = \frac{1}{2} \tilde{u}^2 \qquad (4.6.2.7)$$

then

$$\dot{V}(t,U) = \tilde{u} \frac{d\tilde{u}}{dt} = - \tilde{u} \frac{dU}{dt} . \qquad (4.6.2.8)$$

Examination of the axial velocity control law yields

$$\frac{dU}{dt} = - 1.29 \quad \text{for} \quad \tilde{u} < - \text{dead band}$$

$$\frac{dU}{dt} = + 0.5 \quad \text{for} \quad \tilde{u} > \text{dead band}$$

$$\frac{dU}{dt} = 0 \qquad \text{for} \quad |\tilde{u}| \leq \text{dead band.}$$

Therefore,

$$\dot{V} < 0 \text{ for } |\tilde{u}| > \text{dead band}$$

$$\dot{V} = 0 \text{ for } |\tilde{u}| \leq \text{dead band}$$

and proves   a) global asymptotic stability [17] of the axial velocity control system as

$$\text{dead band} \rightarrow 0$$

and

b) the control law $\in$ M for dead band ≤ 0.2 rad/sec.

Dead band is chosen as 0.18 m/sec because it meets the performance specifications. As the dead band is reduced below this level, the required propellant mass increases. At the same time, it should not be any larger than 0.18 m/sec because variations in the thrust level or LREP mass could result in axial velocities outside the specified 0.2 m/sec performance band.

4.7 General Design

The control algorithms described in Section 4.6 can easily be applied to LREP's with inertias and spin rates other than those specified in Chapter 2. The LREP can be characterized by its spin rate, P, and inertia ratio, I_r, where the inertia ratio is defined as

$$I_r = \frac{I_u}{I_v} .$$ (4.7.1)

The attitude control law's dead band, for the general case, can be specified as

$$\text{dead band}_{Q,R} \leq I_r P \tan\theta_c .$$ (4.7.2)

where θ_c = maximum allowable coning angle given in the specifications. Equation 4.7.2 is based on Equation 4.6.1.1 and 4.6.1.3.

The state estimator optimal feedback matrix, H, can be chosen for the general case such that the estimation error dynamics are equivalent. Therefore, H must be chosen such that the eigenvalues of A-HC are the same as those specified in Section 4.5, for the general A and C. From Equation 4.4.3, the general dynamics matrix is given by

$$A = \begin{bmatrix} 0 & a \\ -a & 0 \end{bmatrix} \qquad \text{where } a = (1 - I_r)P .$$ (4.7.3)

The general measurement matrix is derived from Equations 4.4.3 and 4.5.1, and is given by

$$C = [\, c \quad 0] \qquad \text{where } c = (2 - I_r)P .$$ (4.7.4)

For $H = [h_1 \quad h_2]^T$, the characteristic equation for the general case is

$$\phi = \det\{\lambda I - A + HC\} = \lambda^2 + h_1(2 - I_r)P\lambda + (1 - I_r)^2 P^2 + h_2(1 - I_r)(2 - I_r)P^2$$ (4.7.5)

and the characteristic equation for the current system is

$$\phi = \lambda^2 + 356.4 \, \lambda + 390.8 \, . \tag{4.7.6}$$

H can be specified as:

$$h_1 = \frac{356.4}{(2 - I_r)P} \tag{4.7.7a}$$

$$h_2 = \frac{390.8 - (1 - I_r)^2 P^2}{(1 - I_r)(2 - I_r)P^2} \tag{4.7.7b}$$

and can be chosen for any I_r and P such that the estimation error dynamics are always identical to those specified in Section 4.5.

The attitude control moment comes from Equation 4.4.3, and is given by

$$\frac{|F| \, r_{eff}}{I_v} = 0.6 \tag{4.7.8}$$

and the axial velocity control force, for the general case, is given by Equation 4.4.5 as

$$\frac{|F|}{m} = 0.5 \tag{4.7.9}$$

where m = mass of the LREP. Combining Equations 4.7.8 and 4.7.9 gives the effective moment arm as

$$r_{eff} = \frac{1.2 \, I_v}{m} \, . \tag{4.7.10}$$

Thus, the thrust magnitude, $|F|$, and the effective moment arm, r_{eff}, can be chosen in terms of the LREP's mass and moment of inertia.

The axial velocity control law's dead band can be chosen by

$$dead \, band_u \leq |U_{nom} - U_{min}| \, . \tag{4.7.9}$$

where U_{nom} = nominal axial velocity, and

U_{min} = minimum allowable axial velocity, as given in the specifications.

Therefore, the control system specified in Chapter 4, although it appeared to be a point design, is actually a general design which can be applied to LREPs of all spin rates and mass properties.

4.8 Simulation Results

All computer simulation programs were written in ACSL [18], and the simulation code is included in Appendix A.

Figure 4.8.1 shows the axial velocity for the uncontrolled LREP. The initial axial velocity is 2.5 m/sec (the ejection velocity). The center of gravity is moving in the x direction (i.e., horizontally) at 2.5 m/sec, but the LREP is pitching up due to the tip-off rate induced by the ejector. The LREP's axial velocity is, therefore, decreasing due to the change in coordinate system. The plume event is assumed to occur 2.0 sec after ejection although the exact time is unknown. This assumption is valid because the LREP's axial velocity is predominantly independent of the plume event's time. The plume gives the LREP forward acceleration, but has little overall effect due to the large tip-off rate which is imparted during ejection.

Figure 4.8.2 shows the axial velocity for the controlled LREP. The spin axis, **u**, of the controlled LREP is approximately parallel to the horizontal axis, **x**, because the LREP's orientation is maintained by the attitude control system. There is an initial negative acceleration because the attitude control system is removing the tip-off rate. The LREP pitches up due to the residual rates left by the attitude control system. This causes a slow decrease in the axial velocity. The center thruster is activated to keep the axial velocity inside the performance boundary when the lower bound set by the dead band is reached. The plume gives the LREP an acceleration directly along the spin axis because the orientation is maintained. The axial velocity is kept within the performance boundary by activating the outer solenoids when the upper bound is reached.
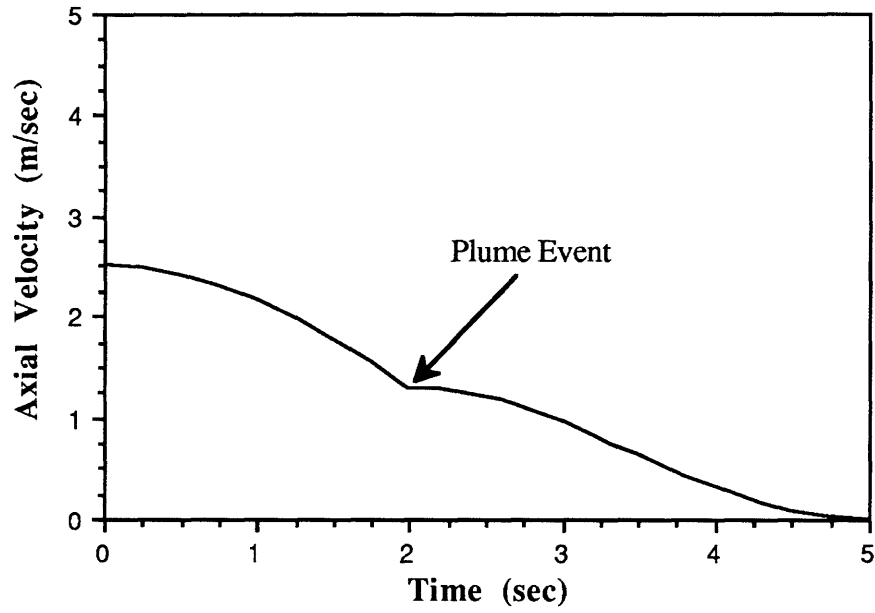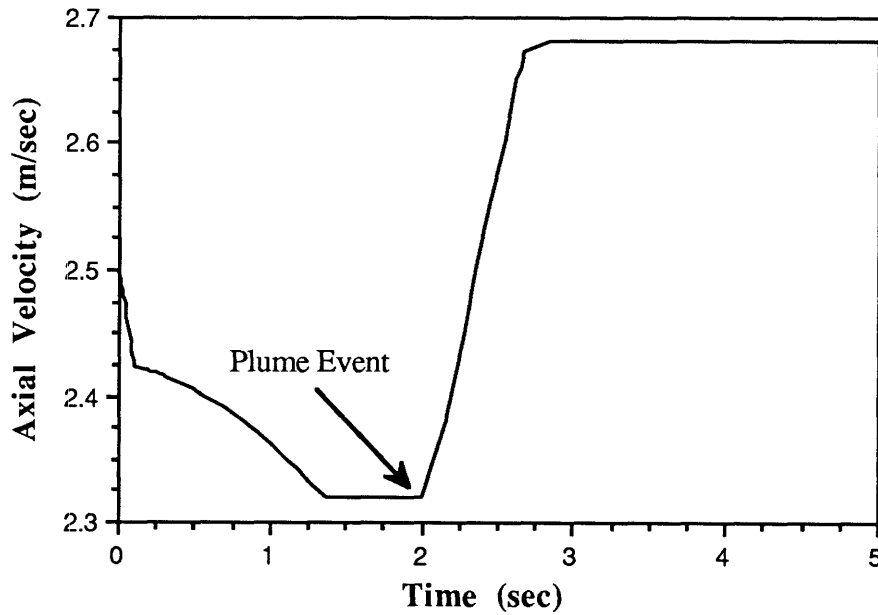
Figure 4.8.1: Uncontrolled Axial Velocity.

Figure 4.8.2: Controlled Axial Velocity.

Figure 4.8.3 shows the coning angle for the uncontrolled LREP. The tip-off rate caused by the ejector gives an initial coning angle of 18°, and the plume event gives an additional 8° of coning. Any lateral rates imparted on the LREP result in a constant coning angle (see Equation 3.4.1) because the LREP dynamics are dissipationless (see Equation 4.5.2).

The coning angle response for the controlled LREP is presented in two sections. The first section presents the coning angle response to the tip-off rate and the second section shows the response to the plume event.

Figure 4.8.4 shows the coning angle tip-off response for the controlled LREP. The attitude control system reduces the initial 18° of coning to below the desired 3° in 100 msec. The plume event response is presented independently because the tip-off coning is removed before the plume event occurs.
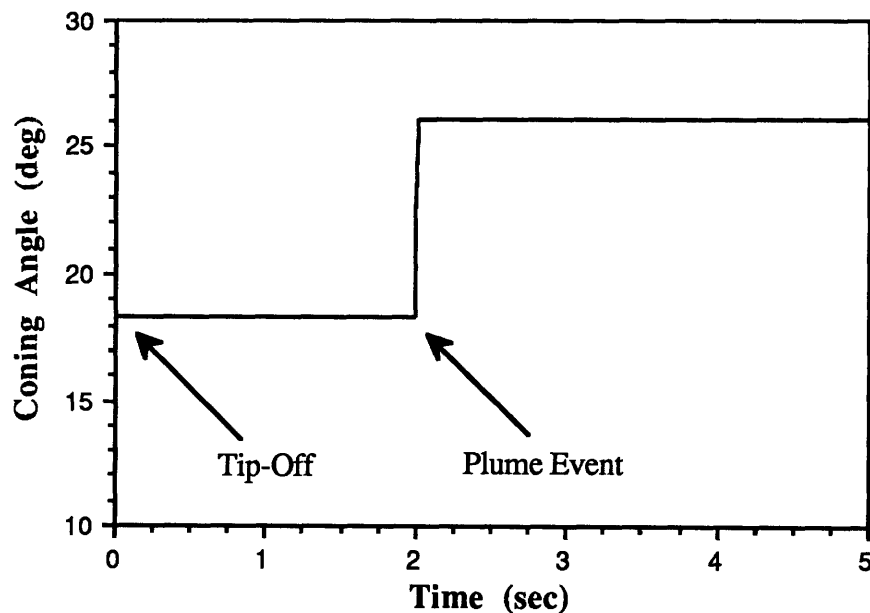

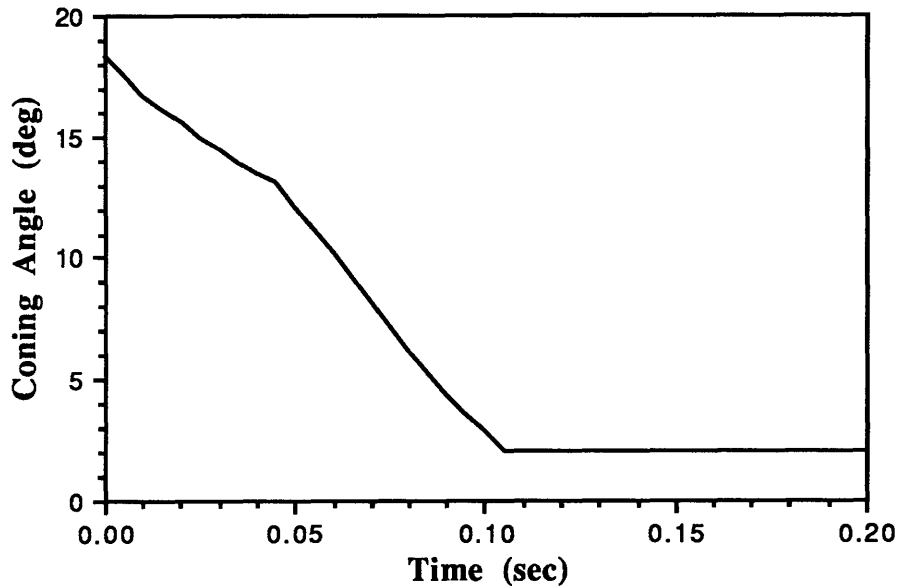Figure 4.8.3: Uncontrolled Coning Angle.

Figure 4.8.4: Controlled Coning Angle Tip-off.

The controlled LREP's response to the plume event is shown in Figures 4.8.5 and 4.8.6. The LREP's orientation during the plume event is unknown, and therefore the axis which the induced moment occurs is also unknown. Figures 4.8.5 and 4.8.6 show the plume event occurring at t = 2.0 sec, but this does not correspond to 2.0 sec after ejection. The plume is shown at t = 2.0 sec for consistency with the previous plots. As described in Section 4.5, the state estimator has a *fast* and *slow* axis of estimation, which implies a best and worst scenario for the plume event response. The worst scenario corresponds to the plume imparting a moment about the w axis, and the best scenario corresponds to the plume imparting a moment about the v axis. The worst scenario shows the coning angle reduced to the desired $3°$ in 1.6 sec, while the best scenario shows the coning angle removed in 50 msec.

Finally, the LREP's pointing angle gives a better understanding of the LREP's motion. The pointing angle is defined as the angle between the spin axis, u, and the horizontal axis, x. The pointing angle for an uncontrolled LREP is shown in Figure 4.8.7. The pointing angle is initially increasing at 3 $°/sec$ (the tip-off rate) and the plume event

increases the rate to 4.3 °/sec. This gives a better understanding of the axial velocity

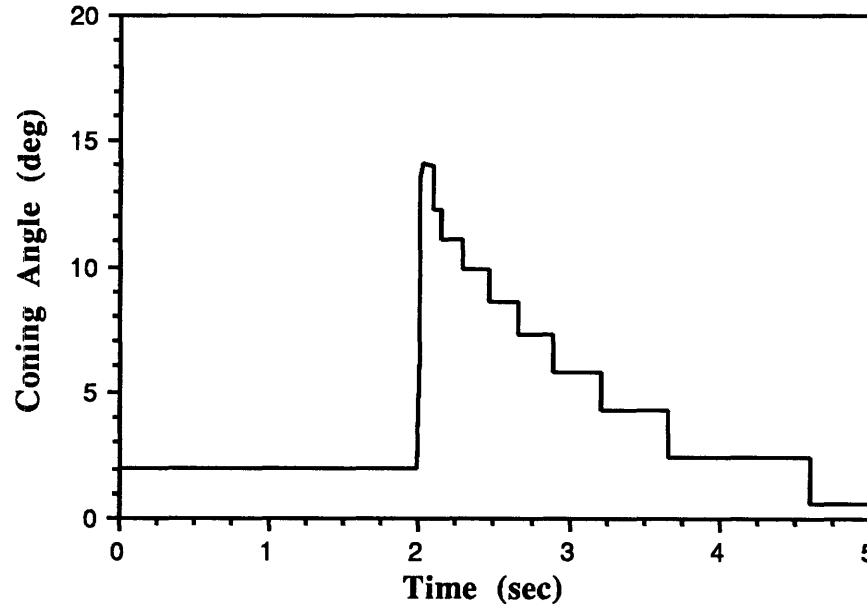response for the uncontrolled LREP.

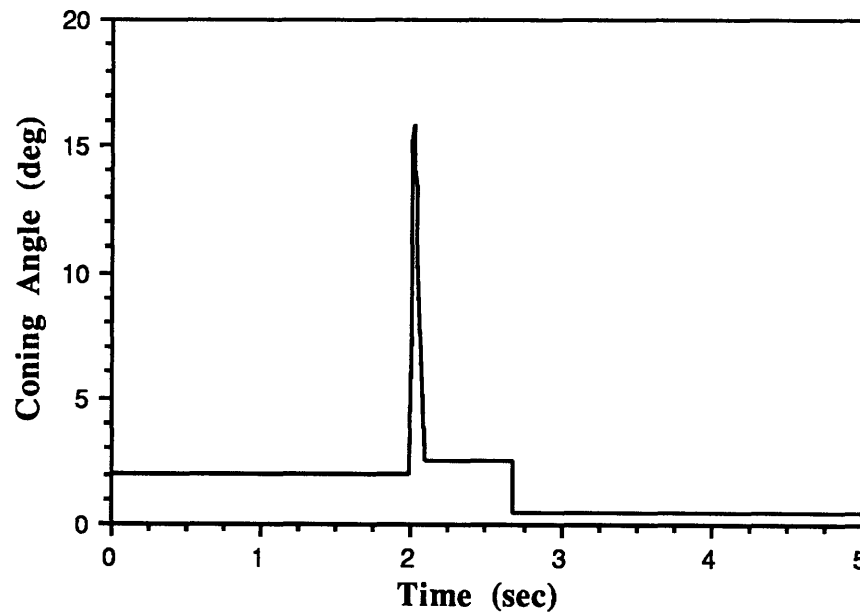**Figure 4.8.5:** Plume Event's Worst Scenario for Controlled Coning Angle.

Figure 4.8.6: Plume Event's Best Scenario for Controlled Coning Angle.

Figure 4.8.8 shows the pointing angle for the controlled LREP. This figure shows that control of the coning angle implies that the orientation of the LREP is maintained. Thus, any latency in coning angle control corresponds to an increase in pointing angle.
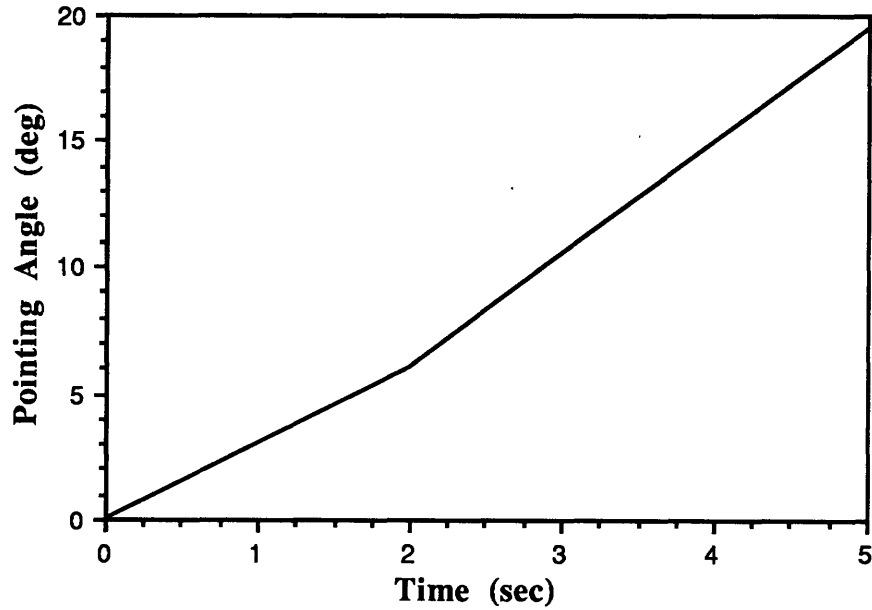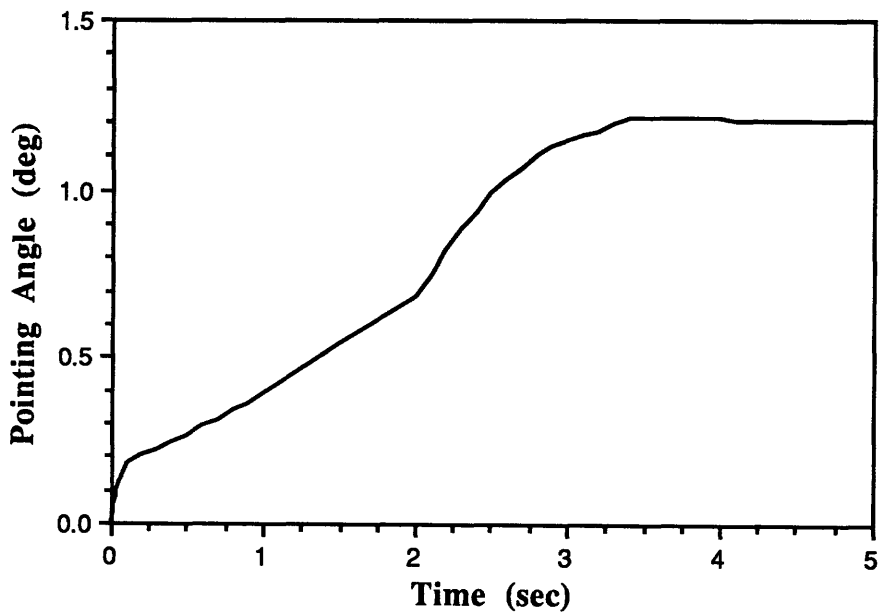

Figure 4.8.7: Uncontrolled Pointing Angle.

Figure 4.8.8: Controlled Pointing Angle.

Chapter 5
Experimental Testing

Control systems are only as good as the model used for their design, and many times these models can neglect a seemingly trivial, but very important aspect of the dynamic system they represent. Therefore, experimental testing is necessary to verify theoretical results. The purpose of these experiments is to verify stability of the attitude control law and to address any practical issues which may have been overlooked.

5.1 Experimental Model

The model used for experimentation represents the LREP's 3 rotational degrees-of-freedom. Any meaningful experiments for axial velocity control would require testing of a free-fall model because the LREP's axial velocity is highly coupled with the rotational dynamics. Therefore, practical considerations limit testing of attitude control only.

The LREP's rotational dynamics are given by Equation 4.4.3 as

$$\frac{dP}{dt} = 0 \tag{4.4.3a}$$

$$\frac{dQ}{dt} = (1 - \frac{I_u}{I_v})P\,R + \frac{|F|\,r_{eff}\,\cos 30}{I_v}\,(L_2 - L_3) \tag{4.4.3b}$$

$$\frac{dR}{dt} = -(1 - \frac{I_u}{I_v})P\,Q - \frac{|F|\,r_{eff}}{I_v}[L_1 - \sin 30(L_2 + L_3)] . \tag{4.4.3c}$$

The experimental model will have the same dynamics as the LREP provided that the conditions

$$(1 - \frac{I_u}{I_v})P = 1.1 \tag{5.1.1}$$

and

$$\frac{|F| \, r_{eff}}{I_v} = 0.6 \qquad\qquad (5.1.2)$$

are satisfied.

Figure 5.1.1 shows the experimental test apparatus and Appendix C gives the detailed drawings for each component. The round plate represents the base plate of the LREP and is attached to a DC motor, which provides the desired spin rate, P. Three thrusters are mounted to the bottom of the plate around the perimeter and the two accelerometers are mounted to the interior of the plate. A motor is attached to a differential-type system which allows the plate to swing freely about two perpendicular axes. The LREP's center of mass corresponds to the intersection of the two differential shafts.

The body-fixed coordinate system is shown in Figure 5.1.2 and the corresponding Earth-fixed system in Figure 5.1.3. u is the motor's spin axis and points upward, v is parallel to the accelerometers and passes through the center of mass, and w is perpendicular to u and v in order to form a right triad. x passes through the intersection of the differential shafts and points upward, while y and z correspond to the differential shafts' directions, as shown in Figure 5.1.3.

The center plate does not contain the entire control system, as the LREP would, because this would require construction of a miniature pressure vessel for the argon gas, mounting the solenoids to the base plate, and powering the system by batteries. This added complexity was considered non-essential to the goals of the experiment. Tubing is required to connect the thrusters to the solenoid valves because the system is not self-contained.
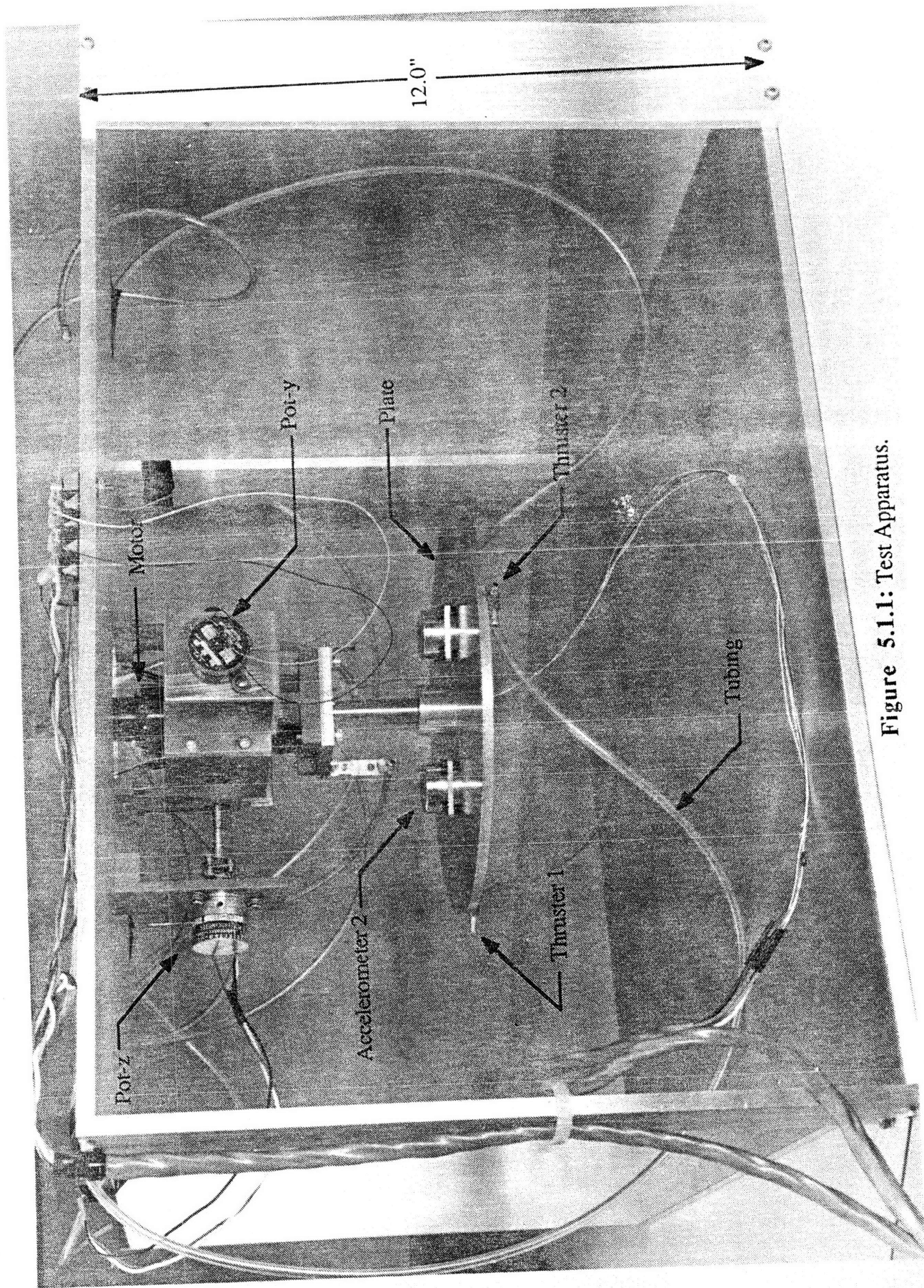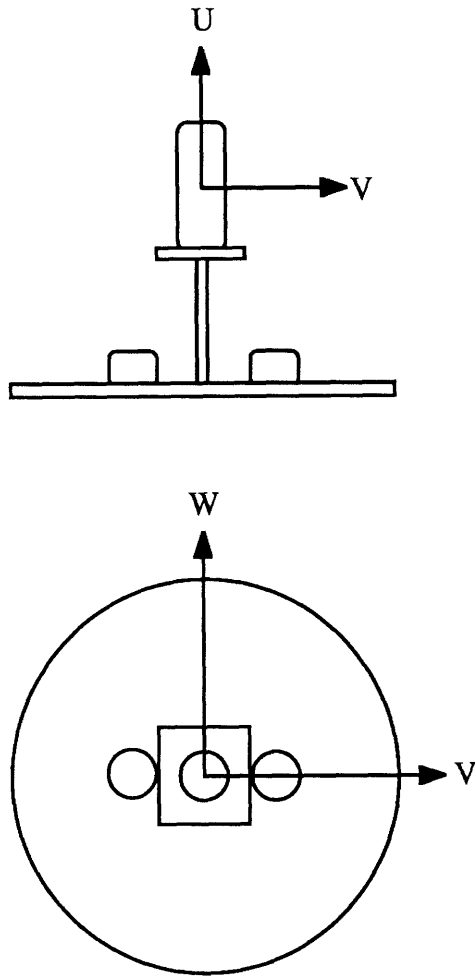
Figure 5.1.1: Test Apparatus.

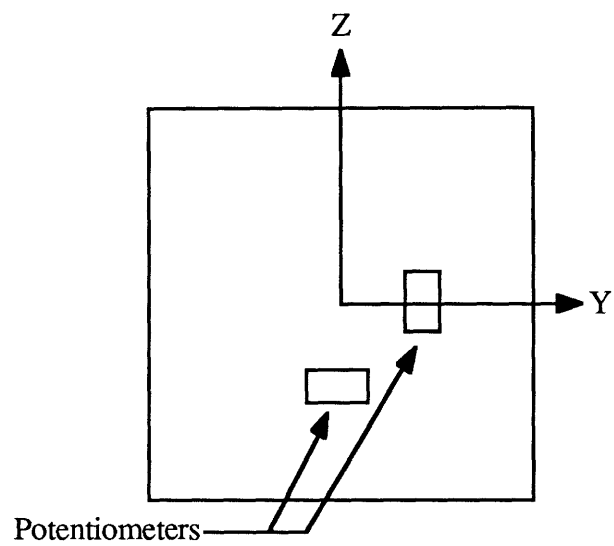**Figure 5.1.2**: Body-Fixed Coordinate System.

Potentiometers

Figure 5.1.3: Earth-Fixed Coordinate System.

The initial design of the test apparatus had a counter-weight mounted to the top of the motor and by removing any gravitational effects, resulted in the desired dissipationless system . However, small forces exerted on the plate by the tubing resulted in significant experimental errors because of the dissipationless system. These errors could not be accounted for in the experiment because they were unrepeatable, and therefore the counter-weight was removed to minimize these errors. However, removal of the counter-weight added additional dynamics to the system because of gravitational contributions to the plate. These new dynamics are referred to as *pendulum* dynamics. The equations of motion must be modified to incorporate the additional dynamics.

The original rotational dynamics were given by Equation 3.2.4 as

$$I_v \frac{dQ}{dt} + (I_u - I_v) \, P \, R = M_v \qquad (5.1.3a)$$

$$I_v \frac{dR}{dt} + (I_u - I_v) \, P \, Q = M_w . \qquad (5.1.3b)$$

For the LREP, M_v and M_w were comprised of the control forces and disturbances only, but the experimental apparatus has additional contributions from gravity and bearing friction. The pendulum model depicted in Figure 5.1.4 is utilized in order to include the additional forces. The equation of motion for the pendulum is given by

$$I \frac{d^2\Theta}{dt^2} = - b \frac{d\Theta}{dt} - gml \sin \Theta \qquad (5.1.4a)$$

where Θ = pendulum angle with respect to vertical,

   I = moment of inertia of the pendulum,

   m = mass of the pendulum,

   l = length of the swing arm, and

   b = friction in the bearing.
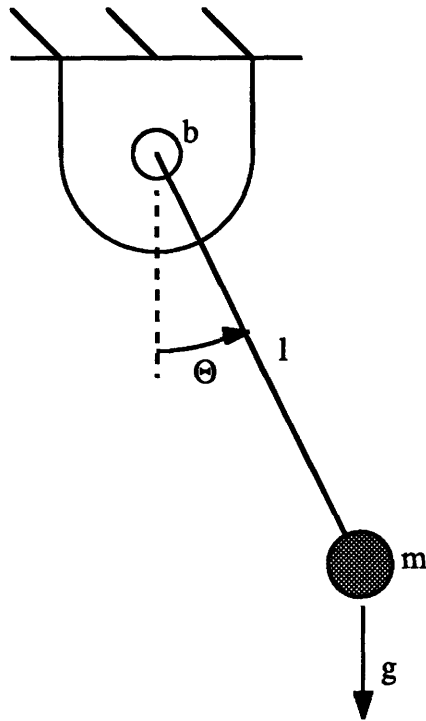
Figure 5.1.4: Pendulum Model.

The linearized pendulum equation is given by

$$I\frac{d^2\Theta}{dt^2} + b\frac{d\Theta}{dt} + gml\,\Theta = 0.$$ (5.1.4b)

This equation assumes that the pendulum is a point mass, and therefore l can be interpreted as the radius of gyration of the pendulum. With this interpretation, the moment of inertia can be expressed as

$$I = m\,l^2$$ (5.1.5)

and the pendulum equation becomes

$$\frac{d^2\Theta}{dt^2} + \frac{b}{m\,l^2}\frac{d\Theta}{dt} + \frac{g}{l}\,\Theta = 0.$$ (5.1.6)

The standard second order dynamic model is

$$\frac{d^2\Theta}{dt^2} + 2\zeta\omega_n \frac{d\Theta}{dt} + \omega_n^2 \, \Theta = 0 \tag{5.1.7}$$

where ω_n = natural swing frequency of the pendulum, and

ζ = damping ratio.

Therefore, the moment of inertia and bearing friction can be expressed as

$$I = \frac{m \, g^2}{\omega_n^4} \tag{5.1.8}$$

and

$$b = 2\zeta \, \omega_n I \, . \tag{5.1.9}$$

The moment of inertia and the bearing friction can be determined experimentally by pushing on the base plate, observing its swinging motion, and computing ω_n and ζ. Figures 5.1.5 and 5.1.6 show the angle of the motor shaft with respect to vertical for perturbations of the base plate about y and z, respectively. Figure 5.1.5 shows a relatively well behaved response, while Figure 5.1.6 shows the nonlinearities caused by the tubing.
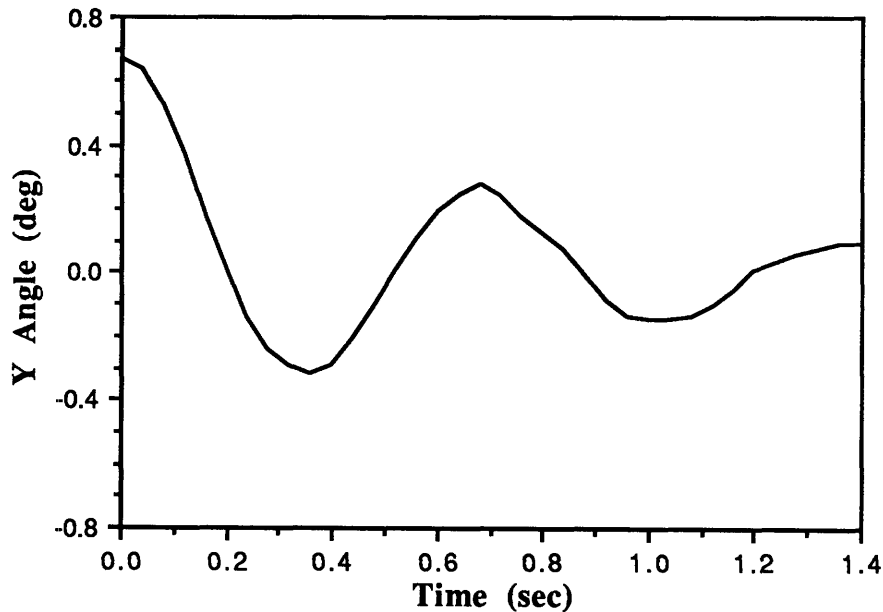

Figure 5.1.5: Base Plate Tapping Response About y.
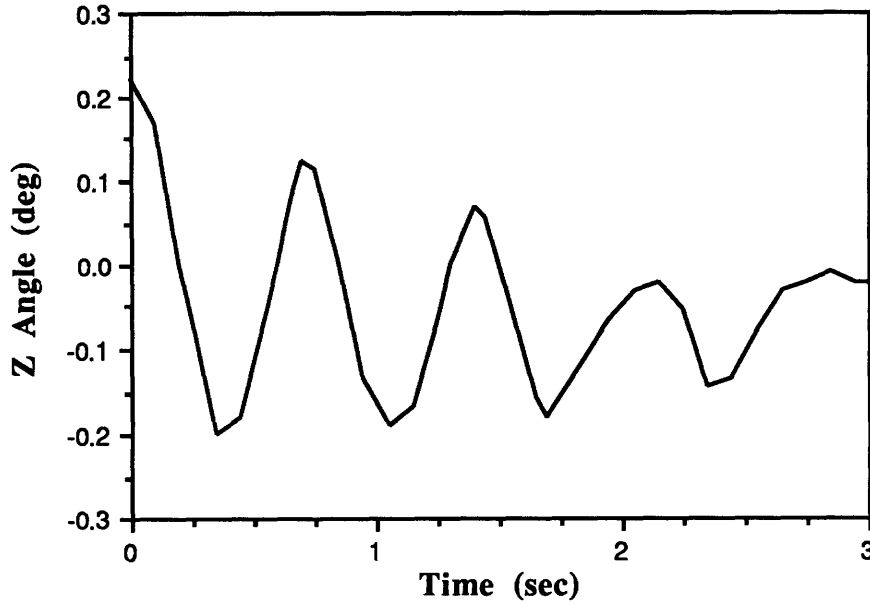
Figure 5.1.6: Base Plate Tapping Response About z.

The period of swing between various peaks is calculated from Figures 5.1.5 and 5.1.6, and shown in Table 5.1.1.

Table 5.1.1: Experimental Swing Periods.

	T_s about y (seconds)	T_s about z (seconds)
peak 1 to 3	.68	.70
peak 2 to 4	.64	.70

The average swing period, T_s, is 0.68 sec, which gives the natural frequency of the test apparatus as

$$\omega_n = \frac{2\pi}{T_s} = 9.2 \text{ rad/sec}$$

and a radius of gyration of

$$l = 0.116 \text{ m}.$$

The total mass of the swinging section is 1.25 kg, which gives the lateral moment of inertia as

$$I = I_v = 0.0168 \text{ kg m}^2.$$

The damping ratio can be determined from the ratio of peaks, assuming a pure second order response, and is calculated from Figure 5.1.5 and shown in Table 5.1.2. The data from Figure 5.1.6 could not be used for the damping ratio calculation because of the guessing involved in extrapolating the necessary information.

Table 5.1.2: Experimental Damping Ratios.

	ζ about y
peak 1 to 3	.13
peak 2 to 4	.11
peak 3 to 5	.17

The average damping ratio is

$$\zeta = 0.137$$

which gives a bearing friction of

$$b = .042 \text{ N m sec.}$$

The bearing friction and lateral moment of inertia fully characterize the test apparatus in terms of the additional *pendulum* dynamics. Two new angles, α and β, must be defined to incorporate this information into the rotational dynamics given by Equation 5.1.3. They are defined as

$$\alpha = \int_0^t Q \ dt \qquad (5.1.10a)$$

$$\beta = \int_0^t R \ dt . \qquad (5.1.10b)$$

Gravity and bearing friction can now be incorporated as part of the applied moments, M_v and M_w. The dynamic equations of motion become

$$I_v \frac{dQ}{dt} + (I_u - I_v) P R = -b\frac{d\alpha}{dt} - gml\, \alpha + |F|\, r_{eff} \cos 30^\circ\, (L_2 - L_3) \qquad (5.1.11a)$$

$$I_v \frac{dR}{dt} + (I_u - I_v) P Q = -b\frac{d\beta}{dt} - gml\, \beta + |F|\, r_{eff} [L_1 - \sin 30^\circ (L_2 + L_3)]\,. \qquad (5.1.11b)$$

Combining Equation 5.1.10 with Equation 5.1.11 yields

$$\frac{d^2\alpha}{dt^2} + \frac{I_u - I_v}{I_v} P \frac{d\beta}{dt} + \frac{b}{I_v}\frac{d\alpha}{dt} + \frac{glm}{I_v}\, \alpha = \frac{|F|\, r_{eff} \cos 30^\circ}{I_v}\, (L_2 - L_3) \qquad (5.1.12a)$$

$$\frac{d^2\beta}{dt^2} - \frac{I_u - I_v}{I_v} P \frac{d\alpha}{dt} + \frac{b}{I_v}\frac{d\beta}{dt} + \frac{glm}{I_v}\, \beta = \frac{|F|\, r_{eff}}{I_v}[L_1 - \sin 30^\circ (L_2 + L_3)]\,. \qquad (5.1.12b)$$

Using the following physical parameters of the test apparatus,

$$m = 1.25 \text{ kg},$$

$$I_u = 0.0024 \text{ kg m}^2, \text{ and}$$

$$r_{eff} = 0.127 \text{ m},$$

| F | and P are chosen as

$$|F| = 0.08 \text{ N}$$

$$P = 73.3 \,^\circ/\text{sec}$$

to meet the criterion specified in Equations 5.1.1 and 5.1.2. The final equations of motion for the test apparatus are found by substituting numbers into Equation 5.1.12 to give

$$\frac{d^2\alpha}{dt^2} - 1.1 \frac{d\beta}{dt} + 2.5 \frac{d\alpha}{dt} + 84.6\, \alpha = 0.5\, (L_2 - L_3) \qquad (5.1.13a)$$

$$\frac{d^2\beta}{dt^2} + 1.1 \frac{d\alpha}{dt} + 2.5 \frac{d\beta}{dt} + 84.6\, \beta = 0.6\, [L_1 - \sin 30^\circ (L_2 + L_3)]\,. \qquad (5.1.13b)$$

The test apparatus dynamics, although not identical to the LREP's rotational dynamics, contain the required dynamics specified in Equation 4.4.3. The control system is identical in structure to the system described in Chapter 4 and only differs by the additional pendulum dynamics which must be included in the state estimator.

5.2 State Estimator

The state estimator is designed using the dynamics specified in Equation 5.1.13. Equation 5.1.13 is converted into state space representation in order to calculate the optimal estimator gains. The state vector is defined as:

$$x = \begin{bmatrix} \alpha \\ \beta \\ Q \\ R \end{bmatrix}. \tag{5.2.1}$$

The measurement comes from the two accelerometers whose sensitive axes are along u. Their locations are

$$r_1 = + 0.038 \ v$$

$$r_2 = - 0.038 \ v.$$

The measurement, in terms of the accelerometer outputs, is given by

$$y = \frac{a_1 - a_2}{.076} \tag{5.2.2}$$

and using the accelerometer equations derived in Section 4.2 yields

$$y = P \ Q - \frac{dR}{dt}. \tag{5.2.3}$$

The state space matrices are

$$A = \begin{bmatrix} 0 & 0 & 1 & 0 \\ 0 & 0 & 0 & 1 \\ -84.6 & 0 & -2.5 & 1.1 \\ 0 & -84.6 & -1.1 & -2.5 \end{bmatrix}$$

and

$$C = [0 \quad 84.6 \quad 2.38 \quad 2.5] .$$

The state estimator is designed by the method described in Section 4.5 and the optimal gain matrix is given by

$$H = [0.03 \quad 0.26 \quad 1.29 \quad 9.10]$$

for

$$G^T = [0 \; 0 \; 1 \; 10] \qquad\qquad V_2 = 1 \qquad\qquad V_3 = 1 .$$

The state estimation error eigenvalues are

$$\lambda_{1,2} = -1.2 \pm 9.0 \, j \qquad\qquad \lambda_{3,4} = -25.2 \pm 15.6 \, j .$$

5.3 Test Configuration and Data Acquisition

A block diagram of the experimental set-up, along with the data acquisition system, is shown in Figure 5.3.1. A picture of the overall experiment is presented in Figure 5.3.2. Two potentiometers are used to measure the rotation angles of the base plate about the two differential shafts. Figure 5.1.3 shows the potentiometer layout and the Earth-fixed coordinate system. The pot which measures the rotations about z, called pot-z, is rigidly attached to the test apparatus structure. See Figure 5.1.1. Pot-y, is attached to the differential system and therefore rotates with the base plate about z.

The coning angle can be directly obtained from these two measurements by selecting the appropriate Euler angles. Using the notation of Section 3.1 and the coordinate system layout described in Section 5.1, the Euler angles, Φ, Θ, and Ψ, are defined by

Φ = rotation about z to form x',y',z'

Θ = rotation about y' to form x'',y'',z''

Ψ = rotation about x'' to form x''',y''',z''' which is the body system u,v,w .

These rotations are classified as a Type 1, 3-2-1 rotation sequence [3]. Therefore, pot-z measures Φ and pot-y measures Θ. As explained in Section 3.1, these angle rotations are functions of the body fixed rotation rates, P, Q, and R. The relationship is given by [3]

$$\frac{d\Phi}{dt} = R\frac{\cos(\Psi)}{\cos(\Theta)} + Q\frac{\sin(\Psi)}{\cos(\Theta)} \tag{5.3.1}$$

$$\frac{d\Theta}{dt} = Q\cos(\Psi) - R\sin(\Psi) \tag{5.3.2}$$

$$\frac{d\Psi}{dt} = P + R\tan(\Theta)\cos(\Psi) + Q\tan(\Theta)\sin(\Psi) . \tag{5.3.3}$$
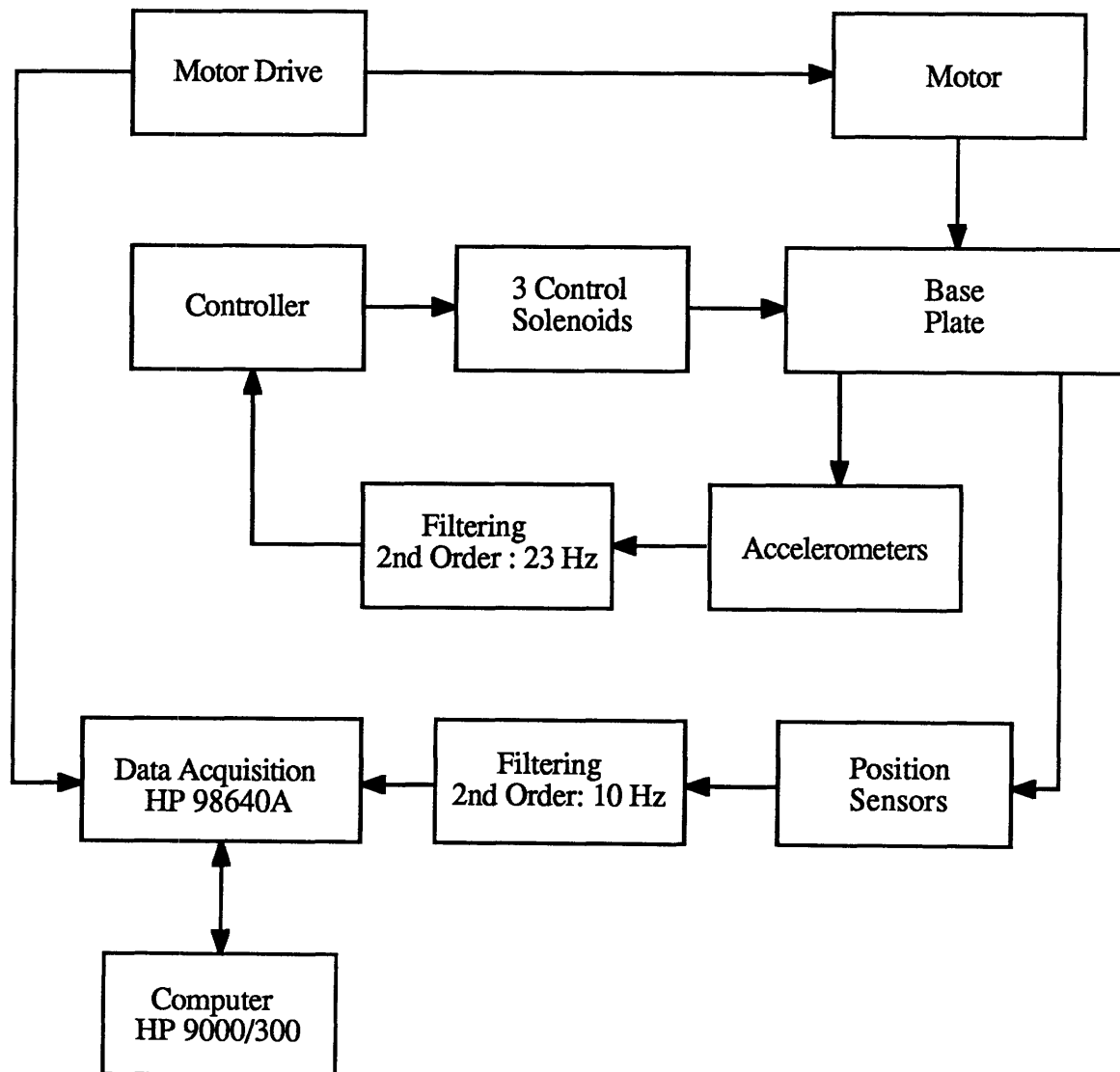
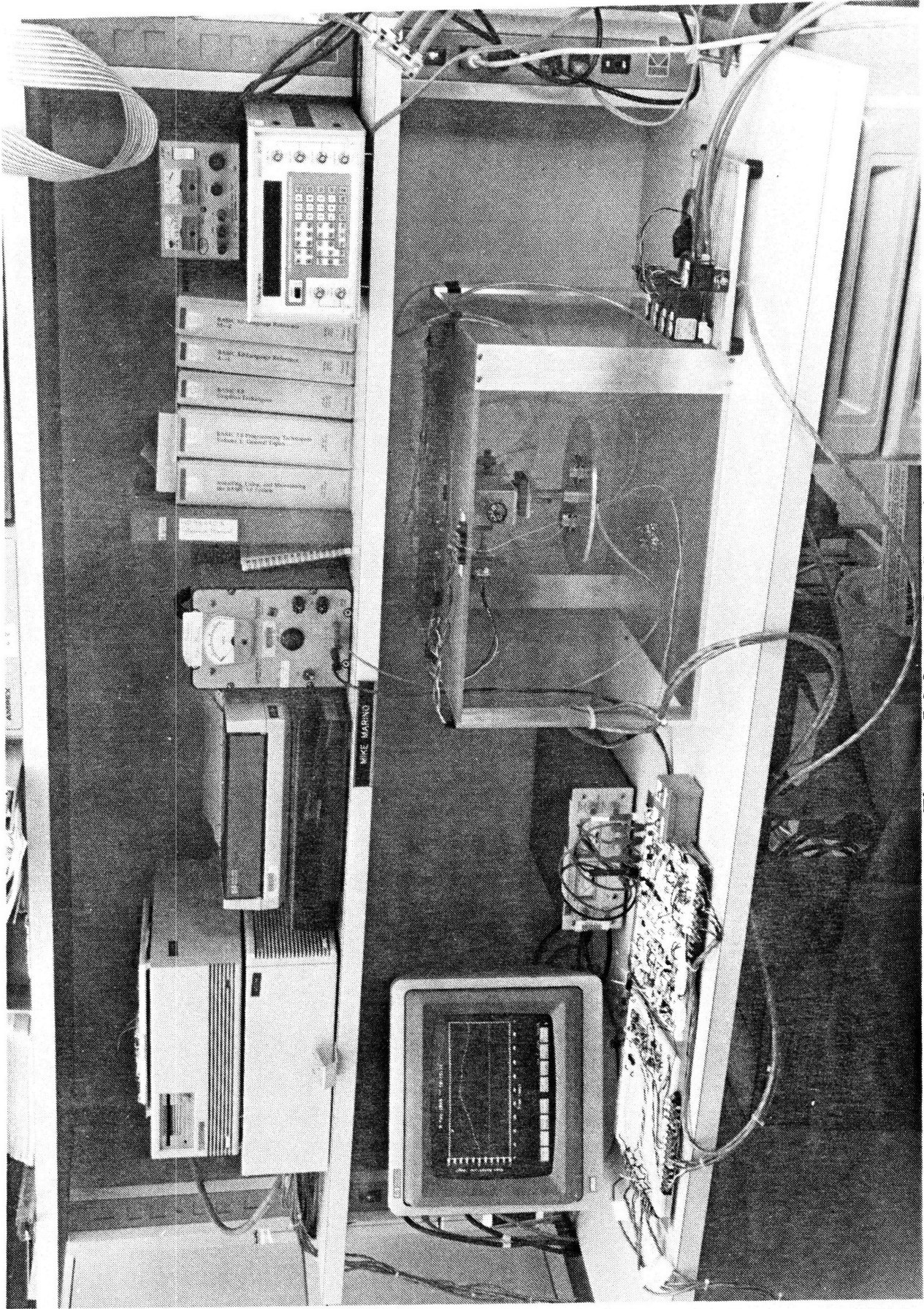**Figure 5.3.1**: Test Configuration Block Diagram.

Figure 5.3.2: Test Configuration.

The coning angle is given in Section 4.6.1 as

$$\sqrt{Q^2 + R^2} = \frac{I_u}{I_v} P \tan(\Theta_c) \qquad (4.6.1.1)$$

for constant spin rate and inertias. A small angle approximation can be used for Θ since the test apparatus allows the base plate to swing a maximum of $\pm 10^\circ$. The Euler derivatives become

$$\frac{d\Phi}{dt} = R \cos(\Psi) + Q \sin(\Psi) \qquad (5.3.4)$$

$$\frac{d\Theta}{dt} = Q \cos(\Psi) - R \sin(\Psi) \qquad (5.3.5)$$

and then

$$\sqrt{(\frac{d\Phi}{dt})^2 + (\frac{d\Theta}{dt})^2} \approx \sqrt{Q^2 + R^2}. \qquad (5.3.6)$$

Therefore, the coning angle can be determined by differentiating both potentiometer measurements and applying Equation 4.6.1.1.

The potentiometer readings were acquired by a Hewlett-Packard 9000/300 computer with a Hewlett-Packard 98640A data acquisition board. The sampling rate for each potentiometer was 100 Hz and corresponds to a Nyquist frequency of 50 Hz. Anti-aliasing filters were needed to attenuate any signals comprised of frequencies above the Nyquist frequency. The transfer function of the anti-aliasing filter, $F(s)$, is

$$F(s) = \frac{62.8^2}{(s + 62.8)^2}. \qquad (5.3.7)$$

As shown in Figure 5.3.1, the data acquisition is completely independent of the control system. Appendix D contains the schematic of the electronics useded in the experiments.

5.4 Experimental Results

The experiment begins with the orientation of the base plate such that y is parallel to -w and z is parallel to v. At t = 0, the motor drive starts the spin rate motor whose initial torque imparts a moment on the base plate and causes precession. The initial configuration is necessary so the disturbance torque is imparted on both v and w. Figure 5.4.1 shows the coning angle for the uncontrolled test. The coning angle initially rises to 29°, but the tubing quickly reduces the coning angle to 10°. The relatively slow decay is due to bearing friction. The pendulum effect causes the coning angle to oscillate whereas the LREP's dissipationless system would maintain constant coning. Nonlinear effects are seen at t = 1.0 sec, where the peak decreases and then suddenly increases, and are also seen by comparing the third and fourth peaks. Peak 4 is larger than peak 3 which indicates that energy is being added to the system. This effect can only be due to the tubing.

Figure 5.4.2 shows the coning angle for a controlled test. During the first 0.5 sec, the controlled response is nearly identical to the uncontrolled response. However, the coning angle is reduced after t = 0.5 sec and is under the specification of 3° at t = 0.8 sec. This result is consistent with the eigenvalues specified in Section 5.2.
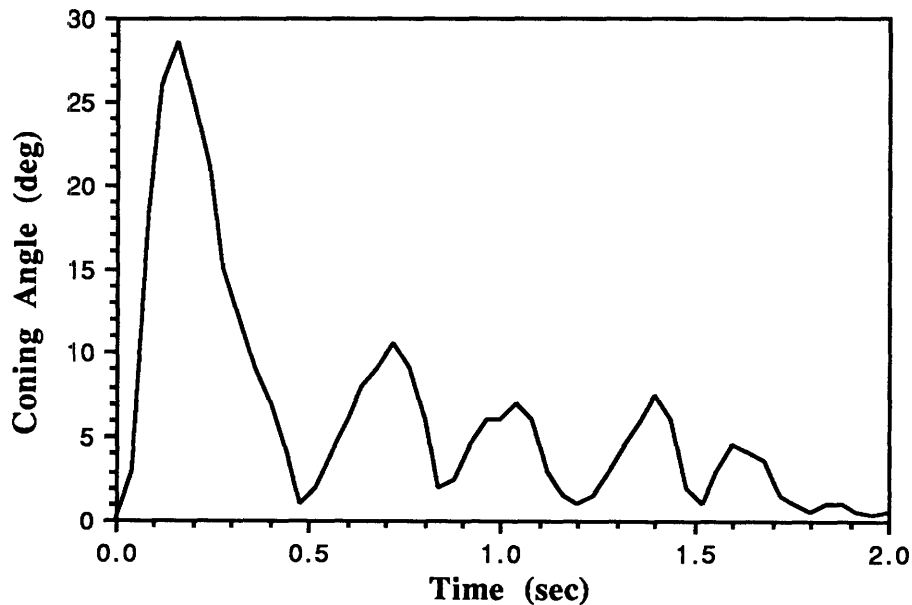

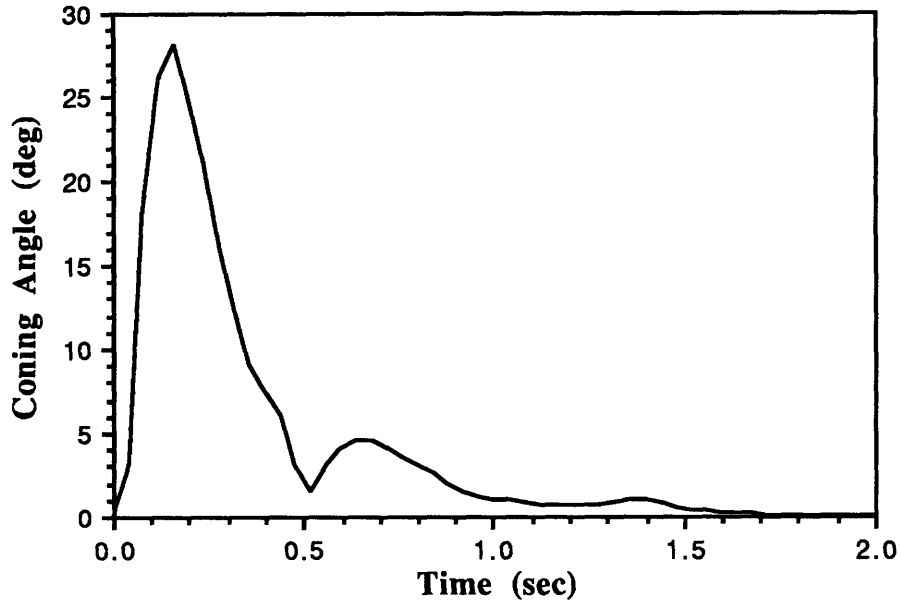**Figure 5.4.1:** Uncontrolled Coning Angle for the Experimental Test.

Figure 5.4.2: Controlled Coning Angle for the Experimental Test.

Many practical issues were addressed during these experiments. The accelerometers made testing impossible during business hours because they can detect any ground vibrations, such as those caused by people walking or equipment turning on. Although the state estimator provided some filtering, an additional filter was needed to further reduce the noise corruption. The filter transfer function is

$$M(s) = \frac{144^2}{(s + 144)^2} \, .$$

(5.4.1)

The solenoid valve interfacing was also a problem. The solenoid specifications gave an *on* time and *off* time of 10 msec for the valve. Initially, a first order filter with a rise time of 10 msec was used to condition L_1, L_2, and L_3 before they were fed back to the estimator. See Figure 5.4.3. This is incorrect because the 10 msec *on* time is actually an energizing time. A problem occurs if L_1, L_2, or L_3 is true for less than 10 msec. The solenoid valves would never turn on but the estimated states are based on these thrusts being applied. The solution is shown in Figure 5.4.4. A monostable flip-flop is used to ensure that every command issued to the solenoids is at least 10 msec in duration. This

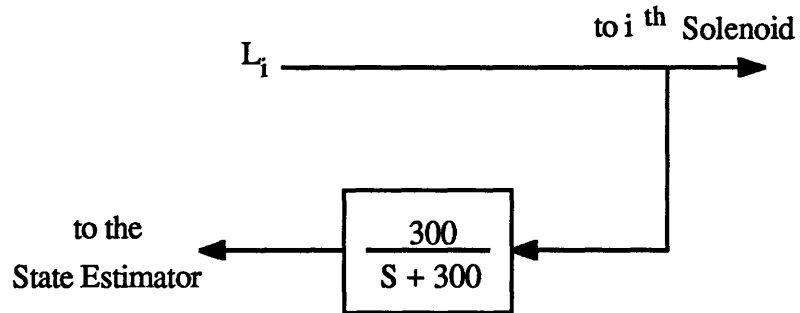experimental result significantly changed the theoretical calculations and simulations shown in Chapter 4.

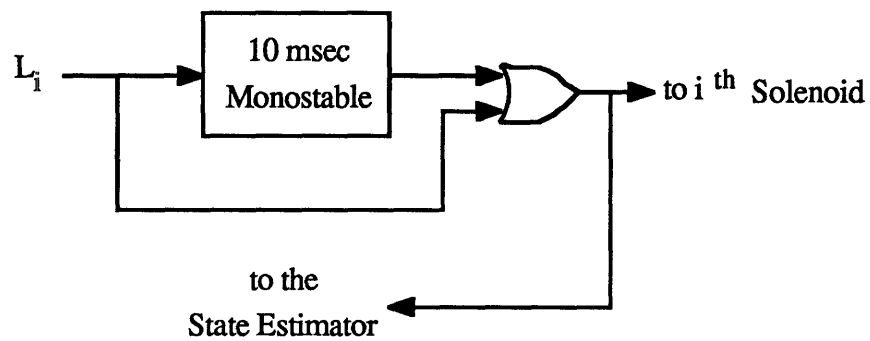**Figure 5.4.3:** Incorrect Processing of the Commanded Thrust Signal.

Figure 5.4.4: Correct Processing of the Commanded Thrust Signal.

Chapter 6
Conclusion

The control system is capable of removing the tip-off rate induced during ejection and the plume induced forces and moments. The LREP's axial velocity is maintained within the bounds specified by the performance criteria, and the coning angle imparted during ejection is reduced below the 3° performance criteria in 100 msec. The plume induced coning angle response is dependent on the orientation of the LREP at the time of interaction. The minimum response time is 50 msec, while the maximum is 1.6 sec. Coning angle control also implies pointing angle control, and the controlled LREP has a pointing angle error less than 1.3^o.

The coning angle of a test apparatus was controlled by the system presented in Chapter 4. The experimental results demonstrate system stability for attitude control. Valuable knowledge about the accelerometers and solenoid valves was obtained from the experiments.

Section 4.7 shows that although this design appears to be a point design, it can be applied to LREP's of any spin rate and inertias by a change of estimator matrices, thrust magnitude, moment arm, and dead bands. These can be calculated by the equations given in Section 4.7 and computer simulated using the program of Appendix A. Therefore, the system is completely general and easy to apply to any type of simple reentry vehicle.

The electronic circuits needed for the LREP system are given in Appendix B. They are based on those used in the experimental tests. The analog building blocks are integrators, amplifiers, and summers. The state estimator's analog signals are converted to digital levels by voltage comparators and digital logic gates are used for control law switching. Power MOSFETs drive the solenoid valves and are activated by logic level FET drivers. The control system electronics require only 21 integrated circuit chips, 11

capacitors, and 67 resistors. The battery/power system is presented in Appendix E and is comprised of 30 batteries and two voltage regulators.

Mass and volume for this system is based on items chosen from manufacturer's catalogs. The parts chosen are not necessarily the smallest or lightest available, but are chosen to demonstrate that mass and volume requirements have been met. Table 6.1 shows the mass and volume for each item. Every item is below the height specification of 30 mm and the total system mass is 0.974 kg. Therefore, all performance criteria specified in Chapter 2 have been met.

Table 6.1: Mass and Volume Breakdown.

Item	Mass (kg)	Dimensions (mm)	Manufacturer and Model No.
2 Accelerometers	0.10	24x25 dia (each)	Sundstrand, QA-700
4 Solenoid Valves	0.38	25x25x51 (each)	Festo, 9712 MNH-3-M5
Tubing	0.018		
Argon Tank	0.002	176x30x30(donut)	custom manufactured
Argon Gas	0.01	--	--
Pressure Regulator	0.084	30x30x58	custom manufactured
20 Batteries	0.10	12.6 dia x 300	Gates, μP80
10 Batteries	0.17	16.8 dia x 280	Gates, 2/3Af
Electronics	0.11	15x100x100	--

Possible future work in the control of lightweight reentry vehicles is virtually unlimited. Modifications to this system may include alternative sensors. Rate sensors eliminate the need for a state estimator, but two of them would be required in addition to the axial velocity accelerometer. This translates to additional power requirements and larger batteries. Therefore, a sensor vs. mass vs. performance trade-off study can be addressed.

Electronics are not the only type of computational hardware available. Fluid signal processors, called fluidics, have been successfully used in attitude stabilization systems. This technology has the advantage that it can operate in very harsh environments. Disadvantages are that fluidic systems have computational limitations and are not as easily modified as electronic systems. However, the possibility of a fluidic control system should also be investigated.

The ejection and plume events are not the only operating regimes. Atmospheric reentry is another source of disturbances that may be addressed in the future. In addition, axial velocity and coning angle may not be the only parameters of interest. Investigation of controlling additional parameters, such as lateral velocity, will provide a challenge for the researcher who attempts to meet the current mass specifications.

References

[1]   David Immerman, MIT Lincoln Laboratory, Aerospace Engineering Group.

[2]   J. L. Meriam, *Engineering Mechanics Volume 2: Dynamics*, John Wiley & Sons, New York, 1978, page 456.

[3]   James Wertz, *Spacecraft Attitude Determination and Control*, D. Reidel Publishing, Holland, 1978, page 765.

[4]   Wertz, page 514.

[5]   Meriam, page 443.

[6]   Meriam, page 434.

[7]   Meriam, page 424.

[8]   Y. M. Timnat, *Advanced Chemical Rocket Propulsion*, Academic Press, Inc., London, 1987, page 4.

[9]   James Davis, MIT Lincoln Laboratory, Control Systems Engineering Group.

[10] Festo Corp., *Pneumatic Products Catalog*, Hauppauge, NY, 1986, page 14.

[11] Huibert Kwakernaak and Raphael Sivan, *Linear Optimal Control Systems*, John Wiley & Sons, Inc., New York, 1972, page 330.

[12] Kwakernaak and Sivan, page 331.

[13] R. E. Kalman and R. S. Bucy, "New Results in Linear Filtering and Prediction Theory", J. Basic Eng., Trans. ASME, Ser. D, 83, 1961, pp 95-108.

[14] Michael Athans, "Lecture Notes on the Kalman Filter", MIT Department of Electrical Engineering and Computer Science, Reference No. 830405/6232, 1983.

[15] Kwakernaak and Sivan, page 346.

[16] Kwakernaak and Sivan, page 371.

[17] M. Vidyasagar, *Nonlinear Systems Analysis*, Prentice-Hall, Inc., Englewood Cliffs, NJ, 1978, page 154.

[18] Mitchell and Gauthier Associates, *Advanced Continuous Simulation Language Reference Manual*, Concord, MA, 1986.

[19] Gates Energy Products, Inc., Gainesville, Fl, Reference No. GEP-0520, 1987.

Appendix A
LREP Simulation Program

'   LREP.CSL'

'   ACSL program for a 6 degree of freedom simulation of an LREP'

'   4 solenoids are used for control'

'   algorithm is bang-bang with deadband'

```
program lrep simulation
        logical         upos,uneg,qpos,qneg,rpos,rneg,roff,l1,l2,l3,l4
```

'   Define the simulation environment'

```
        cinterval       cint = .005
        algorithm       ialg = 5
        maxterval       maxt = .0005
        minterval       mint = .005
        nsteps          nstp = 1
```

'   Declare Constants'

```
        constant        g = 9.8,        mass = 3.0,     isp = 51.0,     icross = -.88  ...
                        ,tstop = 5.0,   ptime = 2.0,    thrst = 1.5                    ...
                        ,b1 = .57,      b2 = .494,      udead = .18,    qdead = .0006 ...
                        ,mu = 1.047,    pc = 1.2,       h1 = 150.0,     h2 = 145.0    ...
                        ,r1 = .9,       r2 = .38
```

'   Initialize variables'

```
        initial
```

```
            p = 1.2565

            qic = .037

            ric = .037

            xic = 0.

            yic = 0.

            zic = 0.

            uic = 2.5

            phiic = 0.

            thetic = 0.

            psiic = 0.

            qest = 0.

            qestd = 0.

            rest = 0.

            restd = 0.

            yest = 0.

            tu = 0.

            tv = 0.

            tw = 0.

            off1 = -1.

            off2 = -1.

            off3 = -1.

            off4 = -1.

end $'of initial'


'
                    Macro for the switching function'
macro swch(out,in,band)

            out = .5*(sign(1.0,in-band) + sign(1.0,in+band))
```

macro end

'   Initial calculations'

reff = f1*cos(mu) + r2*sin(mu)

'   Start the integration'

dynamic

derivative

'   Plume Event'

plfx = rsw(t.ge.ptime, 3.6*exp(-(t-ptime)*.8), 0.)

plfy = rsw(t.ge.ptime, .72*exp(-(t-ptime)*.8), 0.)

plmomt = rsw((t.ge.ptime).and.(t.lt.(ptime+.01), 7.0, 0.)

'   Mass and moment of inertia decreasing as the propellant is used'

mass = mass0 - mprop

iu = .08133*mass

iv = iu/.12

iw = iu/.12

'   ----------   Control system   ----------'

'   Accelerometer Measurement for Attitude Control'

ymeas = p*q - rd

'   State Estimator'

procedural(qest,rest = ymeas)

        yest = 2.36*qest + b1*(t1 - .5*(t2+t3))/thrst

        u1 = b2*(t2-t3)/thrst + h1*(ymeas - yest)

        u2 = -b1*(t1-.5*(t2+t3))/thrst + h2*(ymeas - yest)

qestd = 1.1*rest + u1

qest = integ(qestd, 0.)

restd = -1.1*qest + u2

rest = integ(restd, 0.)

end $'of procedural'

'   Axial Velocity Error'

uerr = uic - u

'   Switching Function'

procedural(upos,uneg,rpos,rneg,roff,qpos,qneg = uswch)

upos = (swch(uerr, udead) .gt. .5)

uneg = (swch(uerr, udead) .lt. -.5)

qpos = (swch(qest, udead) .gt. .5)

qneg = (swch(qest, udead) .lt. -.5)

rpos = (swch(rest, udead) .gt. .5)

rneg = (swch(rest, udead) .lt. -.5)

roff = (abs(rest) .lt. .qdead)

end $'of procedural'

'   Thruster Decision Making'

l1 = uneg.or.rpos.or.(qpos.and.roff)

l2 = uneg.or.qneg

l3 = uneg.or.rneg.or.(qpos.and.roff)

l4 = upos

'   Convert the logical variables into the cooresponding 10 msec *on*'

'   time and 10 msec *off* time'

off1 = rsw(l1.and.(t.ge.off1), t+.01, off1)

off2 = rsw(l2.and.(t.ge.off2), t+.01, off2)

off3 = rsw(l3.and.(t.ge.off3), t+.01, off3)

off4 = rsw(l4.and.(t.ge.off4), t+.01, off4)

t1 = rsw(t.lt.off1, thrst, 0.)

t2 = rsw(t.lt.off2, thrst, 0.)

t3 = rsw(t.lt.off3, thrst, 0.)

t4 = rsw(t.lt.off4, thrst, 0.)

'   Convert Solenoid Forces Into Body Forces and Moments'

tu = t4 - (t1+t2+t3)*sin(mu)

tv = (t1 - .5*(t2+t3))*cos(mu)

tw = .866*(t2 - t3)*cos(mu)

momv = .866*(t2 - t3)*reff

momw = (-t1 + .5*(t2+t3))*reff

'   ----------   6 degree of freedom model   ----------'

'   Rotation Rates'

qd = -icross*p*r + (momv + plmomt*vz)/iv

q = integ(qd, qic)

rd = icross*p*q + (momw + plmomt*wz)/iw

r = integ(rd, ric)

'

Euler Angles'

phid = (q*cos(psi) - r*sin(psi))/cos(theta)

phi = integ(phid, phiic)

thetad = q*sin(psi) + r*cos(psi)

theta = integ(thetad, thetic)

psid = p - (q*cos(psi) - r*sin(psi))*tan(theta)

psi = integ(psid, psiic)

'

Translational Velocities'

ud = -q*w + r*v + g*uz + (tu + plfx*ux + plfy*uy)/mass

u = integ(ud, uic)

vd = -r*u + p*w + g*vz + (tu + plfx(vx + plfy*vy)/mass

v = integ(vd, vic)

wd = -p*v + q*u + g*wz + (tw + plfx*wx + plfy*wy)/mass

w = integ(wd, wic)

'

Direction Cosine Matrix Elements'

ux = cos(phi)*cos(theta)

uy = sin(theta)

uz = -sin(phi)*cos(theta)

vx = -cos(phi)*sin(theta)*cos(psi) + sin(phi)*sin(psi)

vy = cos(theta)*cos(psi)

vz = sin(phi)*sin(theta)*cos(psi) + cos(phi)*sin(psi)

wx = cos(phi)*sin(theta)*sin(psi) + sin(phi)*cos(psi)

wy = -cos(theta)*sin(psi)

wz = -sin(phi)*sin(theta)*sin(psi) + cos(phi)*cos(psi)

'   ----------   Additional Information   ----------'

'   Axial Distance Off The Post-Boost Vehicle'

xd = u*uy + v*vy + w*wy

x = integ(x, 0.)

'   Pointing Angle'

point = 57.3*sqrt(phi**2 + theta**2)

'   Coning Angle'

cone = 57.3*atan2(sqrt((iv*q)**2 + (iw*r)**2),   ...

          sqrt((iu*p)**2 + (iv*q)**2 + (iw*r)**2))

'   Propellant Mass'
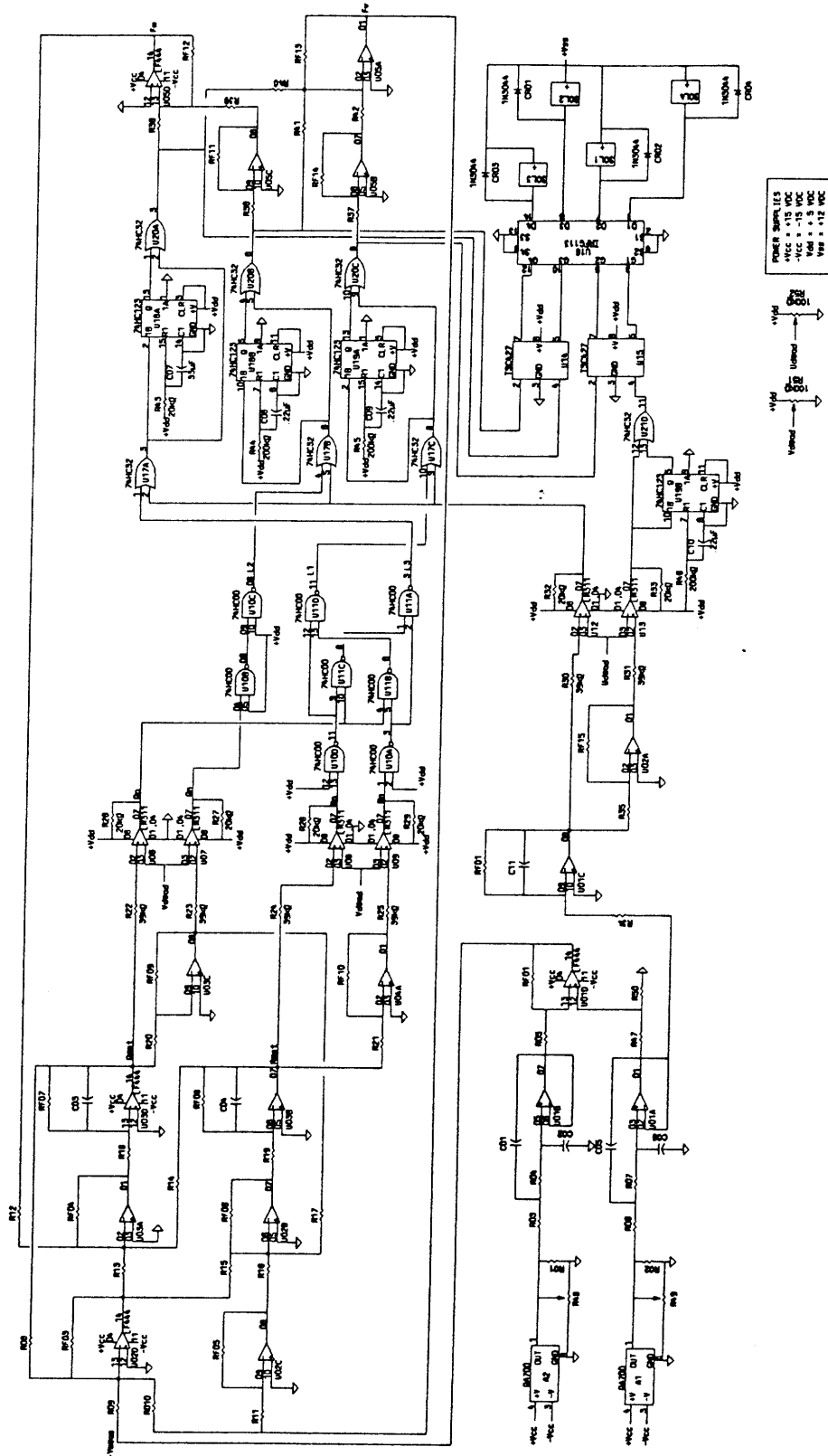
mprop = 1.0/(g*isp) * integ(t1+t2+t3+t4, 0.)

'   Power Consumed By the Solenoids'

energ = integ(pc*(rsw(l1, 1.0, 0.) + rsw(l2, 1.0, 0.) + ...

          rsw(l3, 1.0, 0.) + rsw(l4, 1.0, 0.)), 0.)

end $'of derivative'

          termt(t .ge. tstop)

end $'of dynamic'

terminal

end $'of terminal'

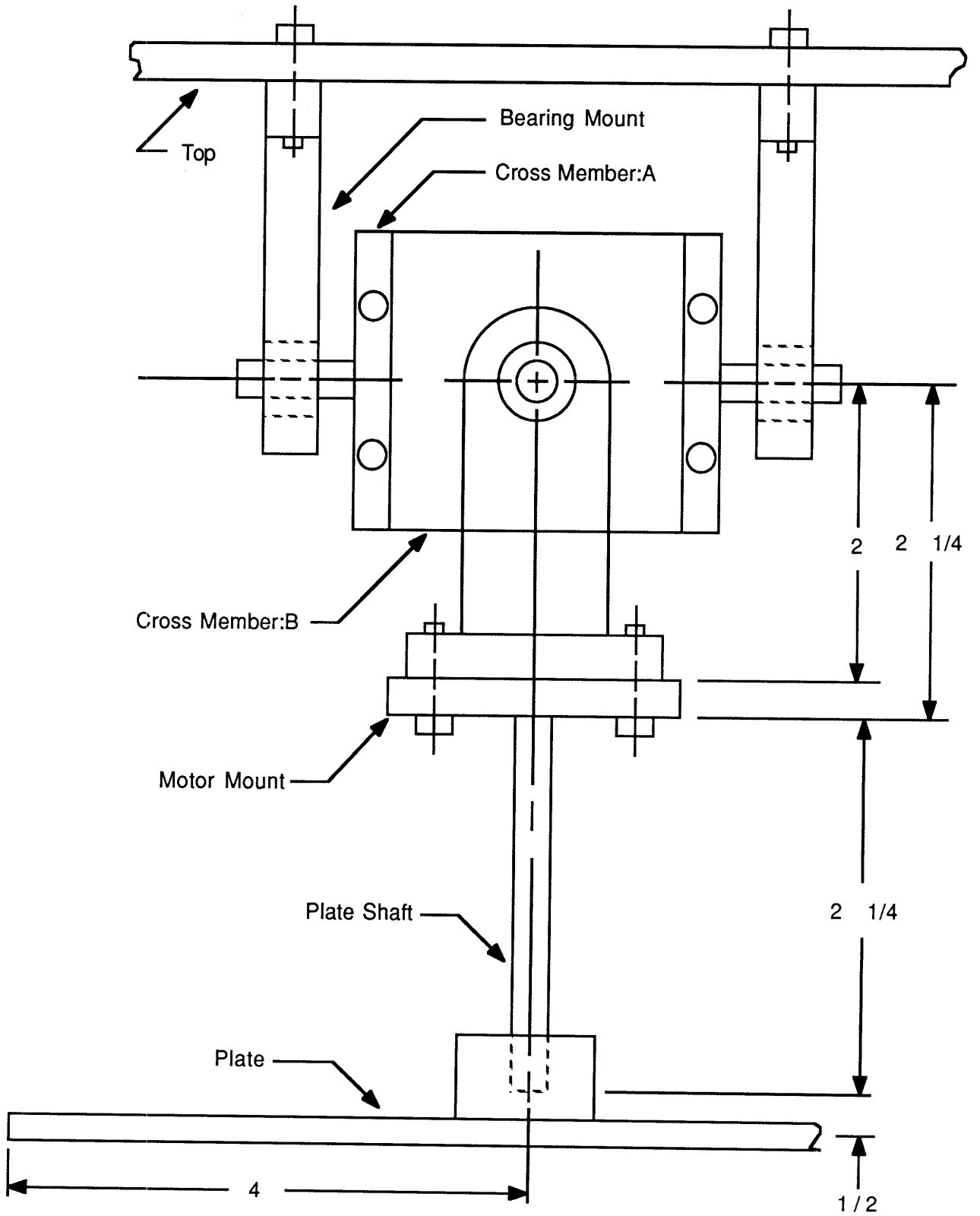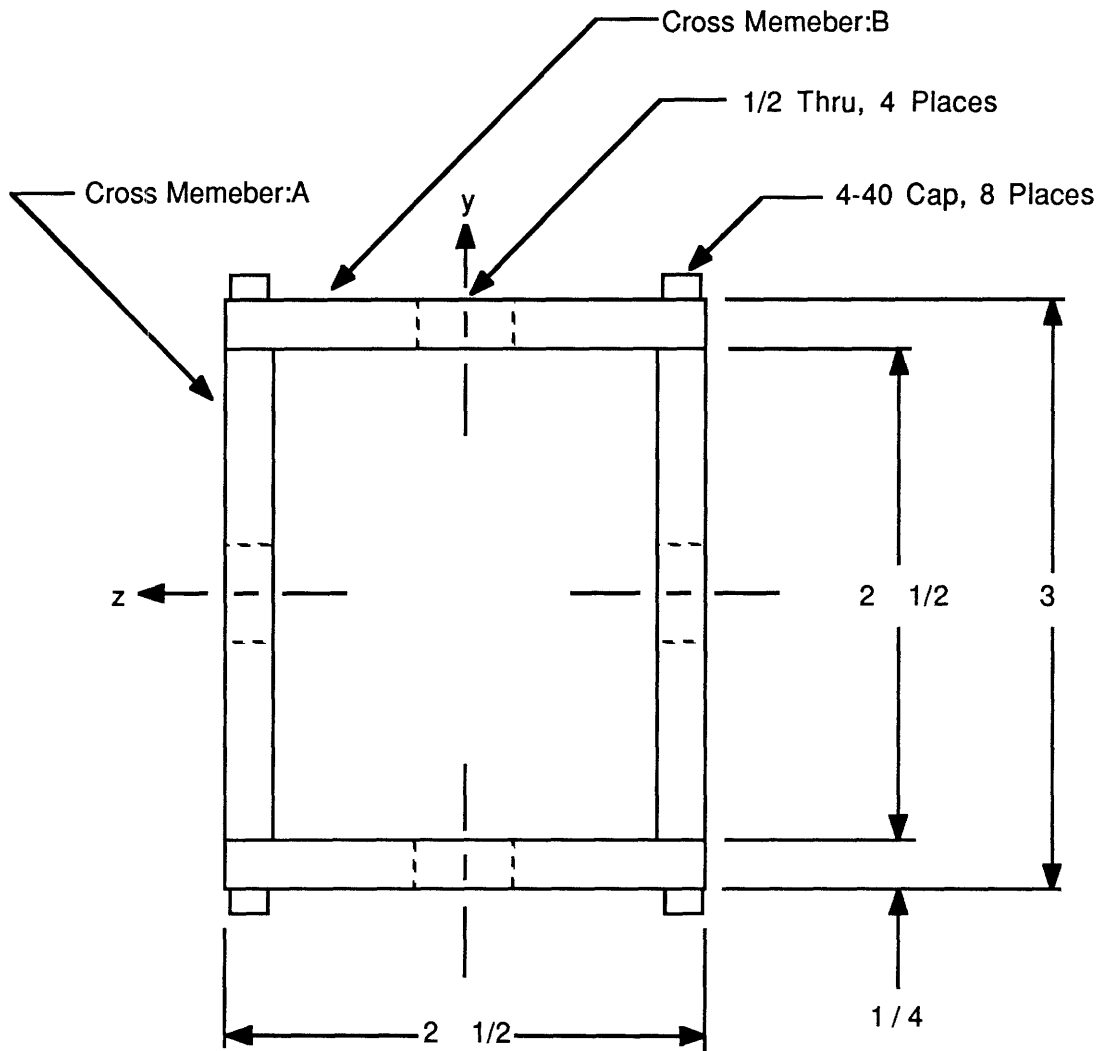end $'of program'

Appendix B
LREP Circuitry

Appendix C
Test Apparatus Drawings

C.1 Motor Mount Assembly

Motor

Motor Mount

Bearing Mount

C.2 Overall Assembly

Top

Bearing Mount

Cross Member:A

Cross Member:B

Motor Mount

Plate Shaft

Plate

2

2   1/4

2   1/4

4

1 / 2
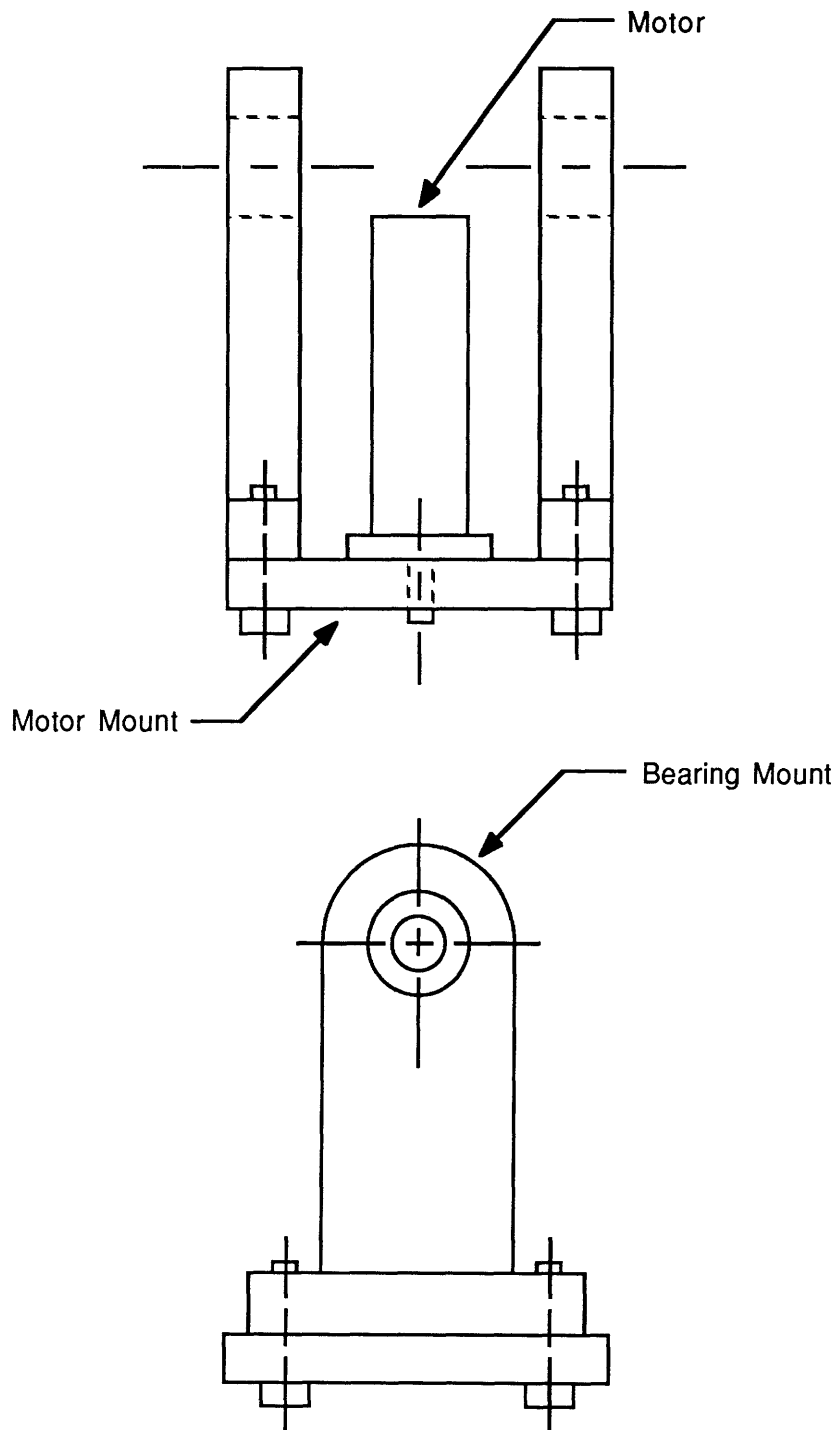
C.3 Upper Yolk Assembly
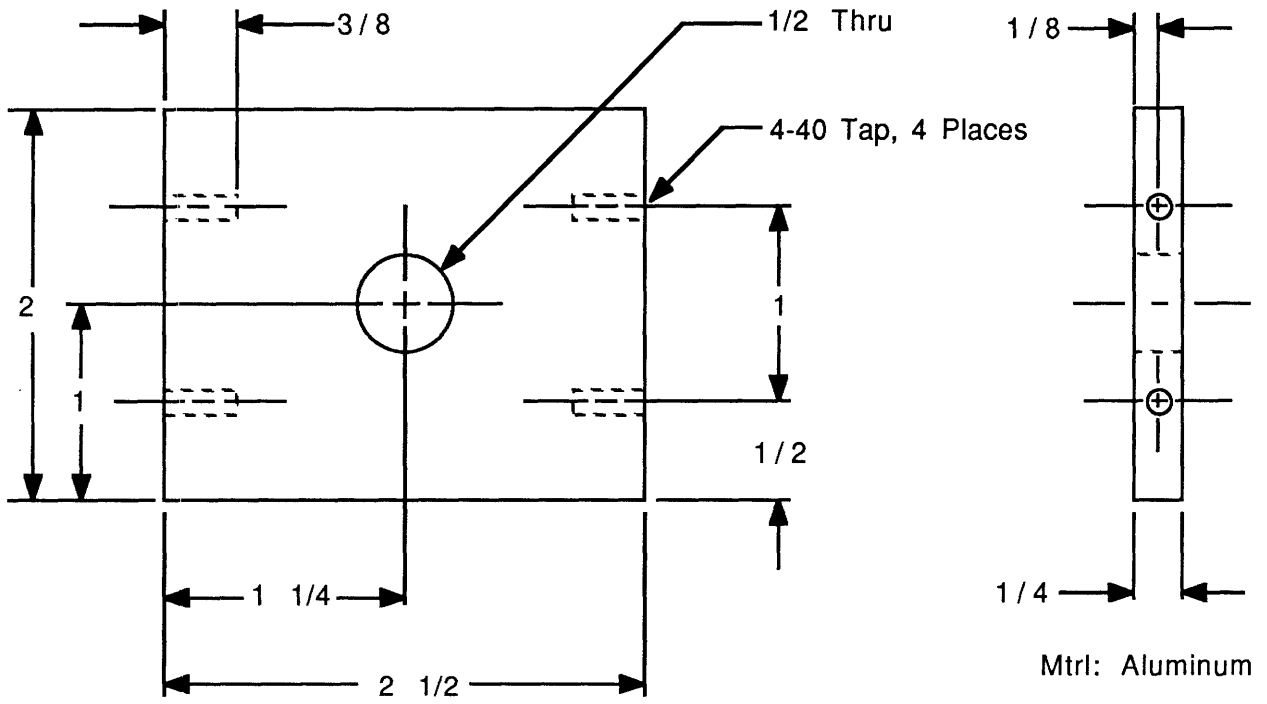
C.4 Plate

8 Dia

1.03 Thru

4-40 Tap, 8 Places

.442

1 1/2

1/4 Thru

3/16

3/4

1
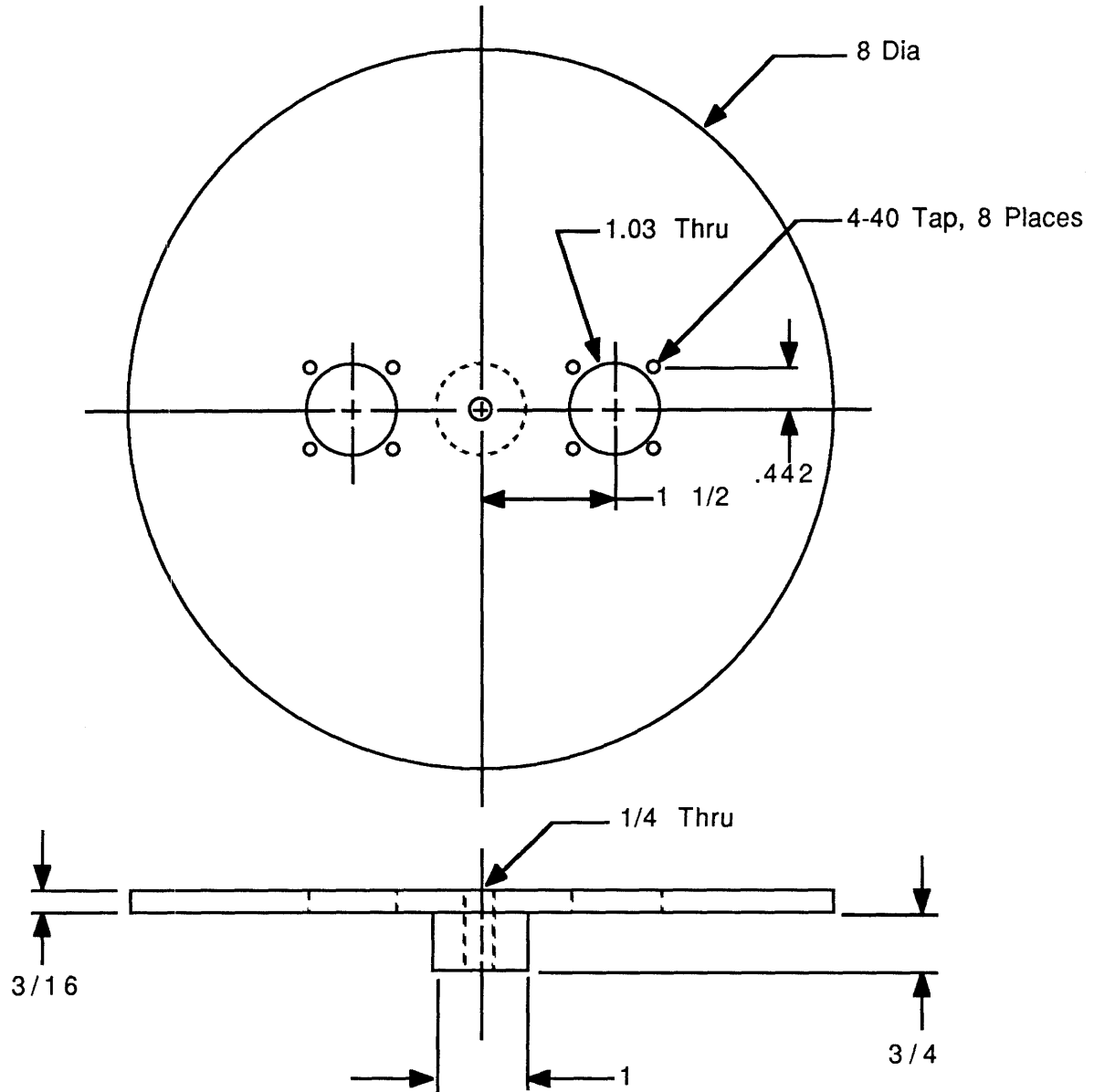
Mtrl: Aluminum

C.5 Motor Mount

1/8 Thru, 4 Places
Centers On A 1" Dia Circle

13/16   Thru

5/32 Thru, 4 Places

1/4

1/4

5/32   5/32

1

2

2

1

2

1/4

Mtrl: Aluminum

C.6 Cross Member A

3/8

1/2 Thru

4-40 Tap, 4 Places

2

1

1

1/2

1 1/4

2 1/2

1/8

1/4

Mtrl: Aluminum

C.7 Cross Member B

1/2 Thru

1/8 Thru, 4 Places

2

1

1

1/2

1/8

1/8

1 1/4

2 1/2

1/4

Mtrl: Aluminum

C.8 Bearing Mount

1 7/16

7/16

15/16

6-32 Tap, 2 Places

1/2 THRU

2 1/2

2

1 1/2

3/16

1 7/8

5/16

3/8

5/32
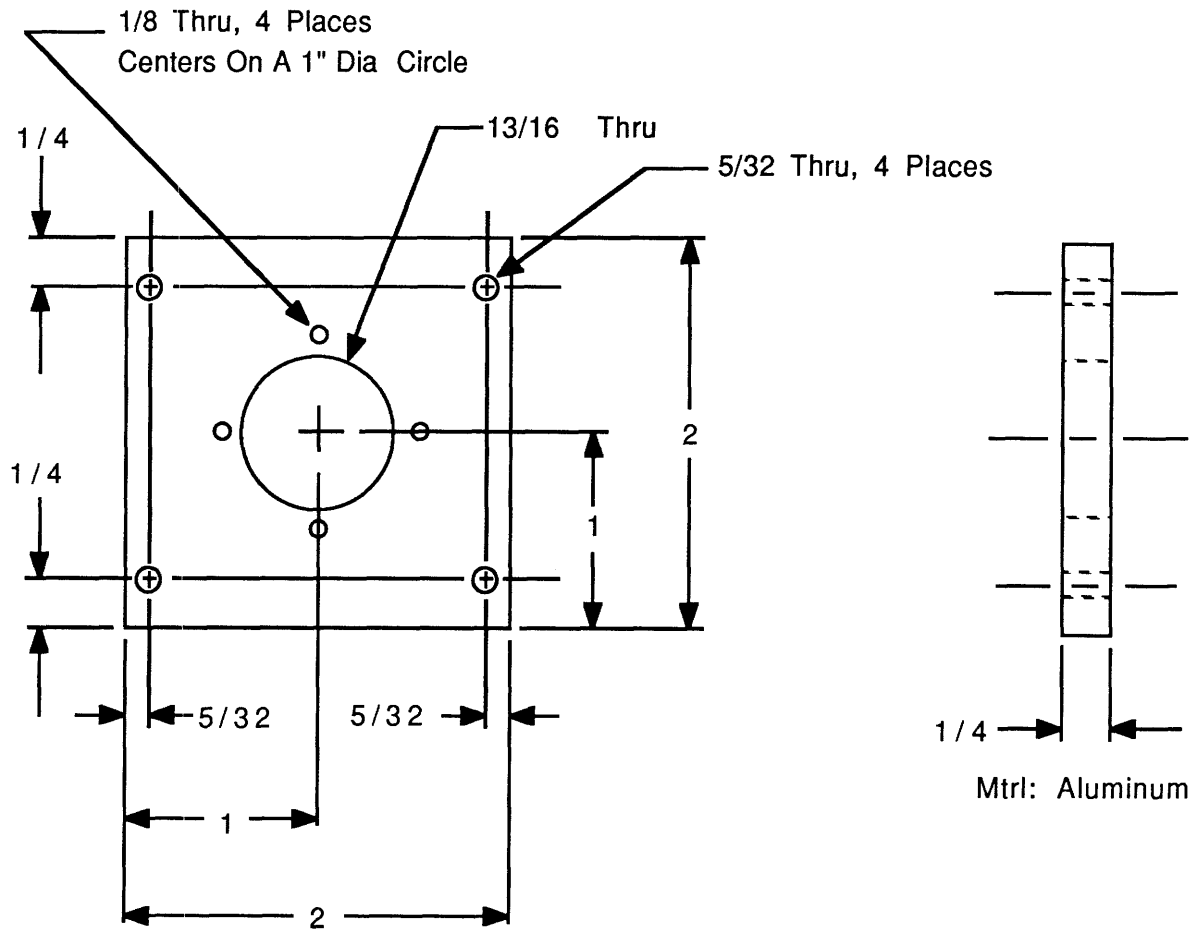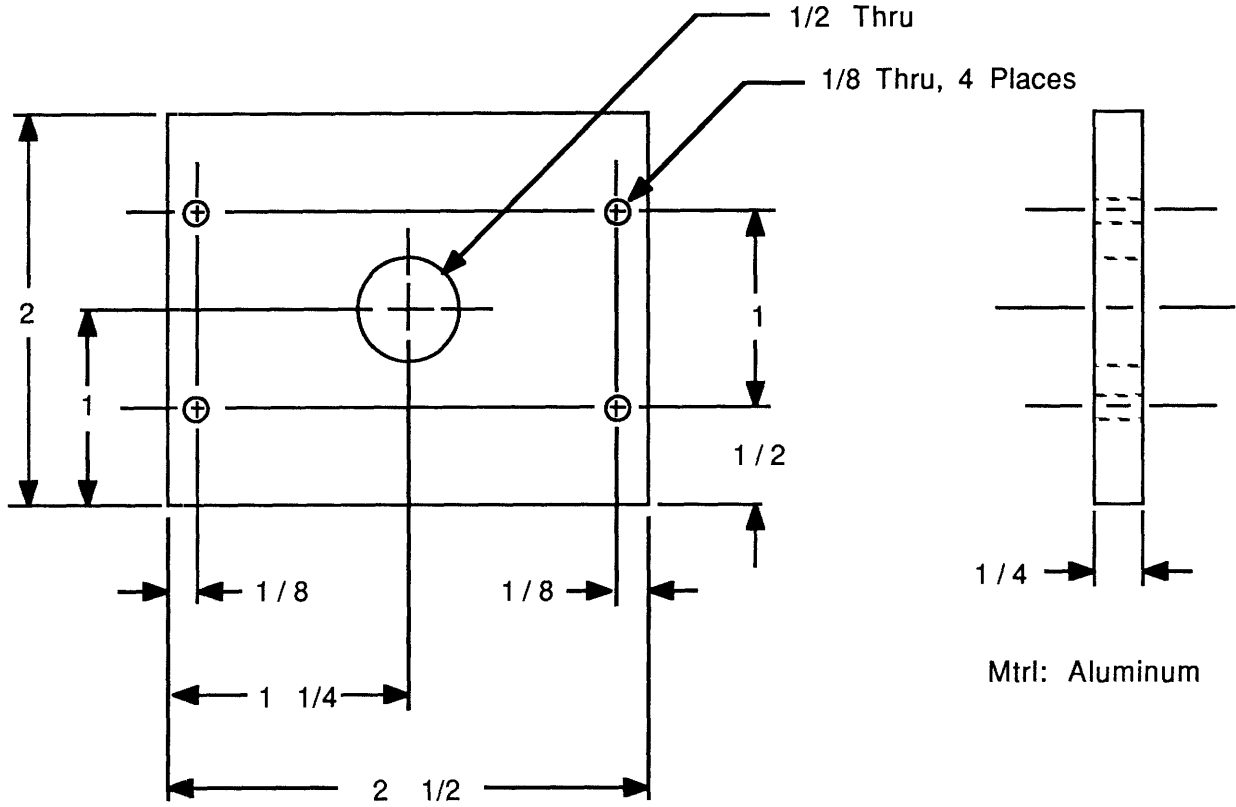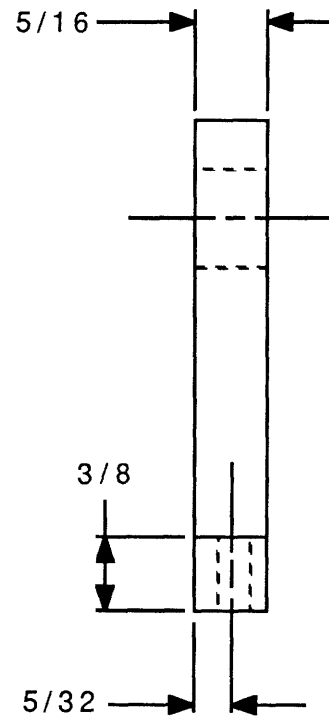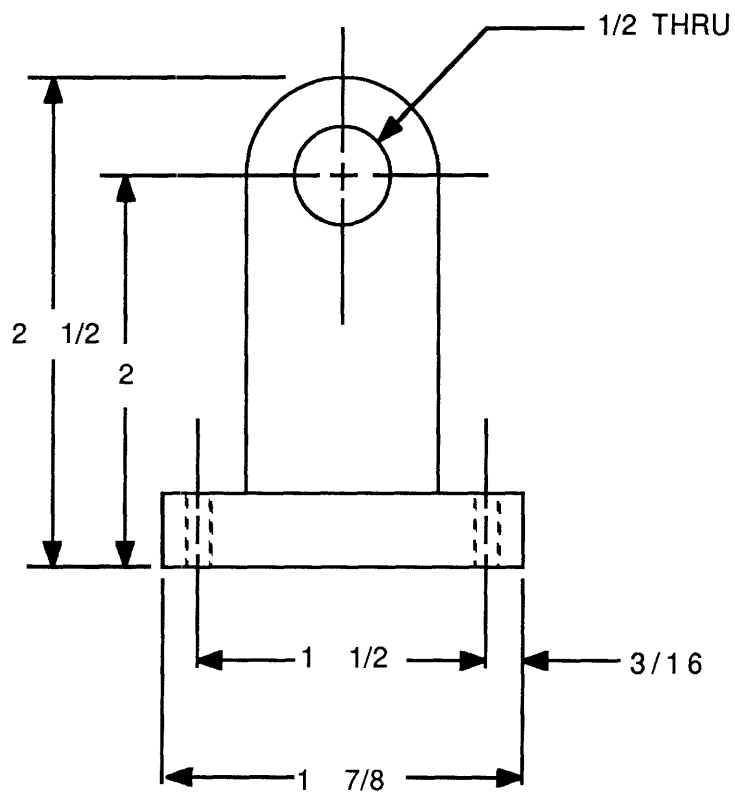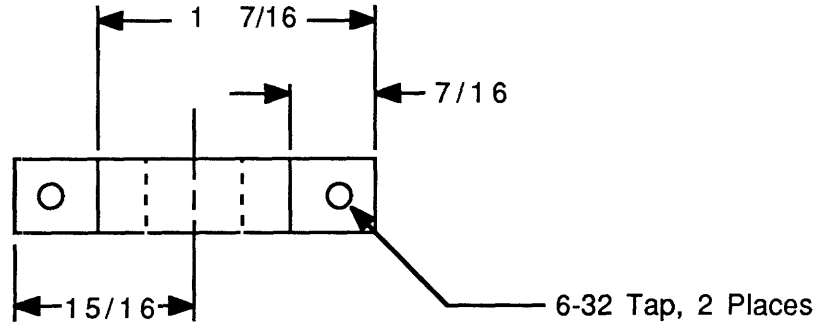
Mtrl: Aluminum

C.9 Plate Shaft

4-40 Tap

1/2 Dia

5/16 Dia

1/4

1 3/4

2 1/4

Mtrl : Aluminum

1/4 Bore, 1/2 Deep

Appendix D
Experimental Circuitry
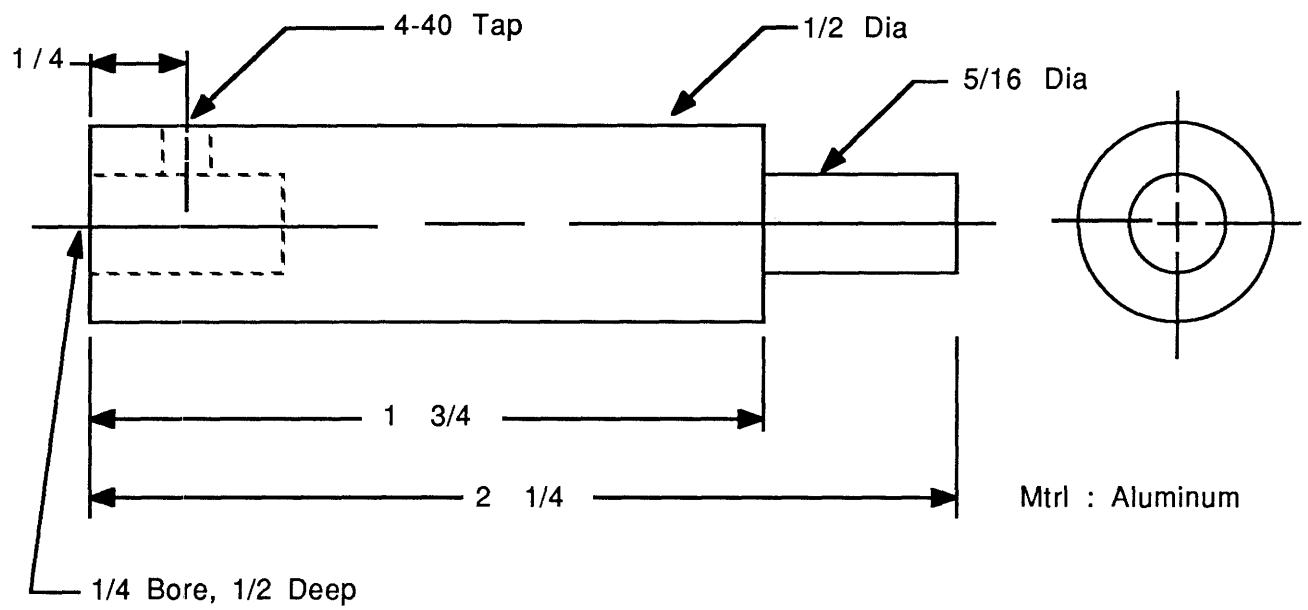
Appendix E

Battery/Power System Design

<u>Required Voltage Supplies</u>

+ 5 VDC for digital @ 0.05 amps

+ 12 VDC for solenoid valves @ 0.375 amps/sol * 3 sol = 1.125 amps

± 15 VDC for analog @ 0.2 amps

<u>Notes:</u>

a) maximum of 3 solenoids are simultaneously energized

b) only ± 15 VDC supplies are regulated

c) assume 50 % efficiency for the voltage regulators

d) minimum operating time = 5.0 sec

e) battery cells are + 1.2 volts each

f) discharge temperature = -30 °C

g) battery information based on GATES NiCd battery cells [19]

h) design is based on the battery configuration in Figure E.1
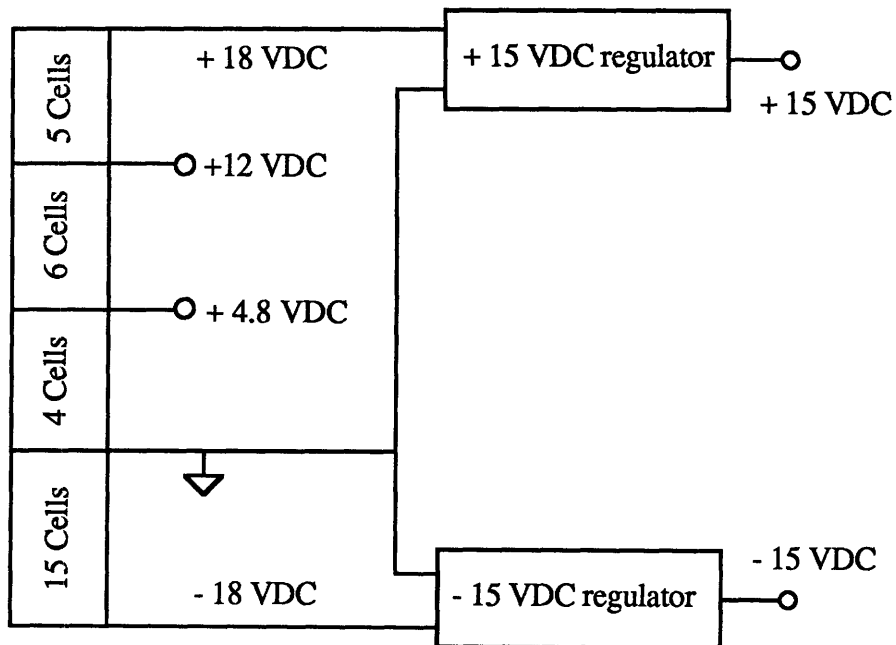

Figure E.1: Battery Configuration.

1) First 10 batteries supply the solenoid valves, digital, and analog

a) total current = $1.125 \text{ A} + 0.05 \text{ A} + \dfrac{0.2 \text{ A}}{50 \text{ \% effeciency}} = 1.575 \text{ A}$

b) use GATES, $\frac{2}{3}$ Af cell: C rating = 0.475 Ahr

c) discharge rate calculation

$$\dfrac{1.575 \text{ A}}{0.475 \text{ C}} = 3.3 \text{ C multiples} \Rightarrow 90 \text{ \% of cell capacity available}$$

d) temperature discharge calculation

discharge at -30 $^{\circ}$C $\Rightarrow$ 20 % of cell capacity available

e) cell lifetime at full discharge rate

$$\dfrac{0.475 \text{ Ahr} * 0.9 * 0.2}{1.575 \text{ A}} = 0.054 \text{ hr} = 195 \text{ sec}$$

2) 20 batteries for supplying analog only

a) total current = $\dfrac{0.2 \text{ A}}{50 \text{ \% effeciency}} = 0.4 \text{ A}$

b) use GATES, μP80 cell: C rating = 0.065 Ahr

c) discharge rate calculation

$$\dfrac{0.4 \text{ A}}{0.065 \text{ C}} = 6.15 \text{ C multiples} \Rightarrow 80 \text{ \% of cell capacity available}$$

d) temperature discharge calculation

discharge at -30 $^{\circ}$C $\Rightarrow$ 20 % of cell capacity available

e) cell lifetime at full discharge rate

$$\dfrac{0.065 \text{ Ahr} * 0.8 * 0.2}{0.4 \text{ A}} = 0.026 \text{ hr} = 94 \text{ sec}$$

3) Mass

$$10 \frac{2}{3} \text{Af cells} * 16.9 \text{ gr/cell} = 169 \text{ gr}$$

$$20 \text{ }\mu\text{P80 cells} * 5.10 \text{ gr/cell} = 102 \text{ gr}$$

$$\text{total battery mass} = 271 \text{ gr}$$

4) Volume

$$\frac{2}{3} \text{Af cell volume} = 28 \text{ mm x } 16.8 \text{ mm diameter}$$

$$\mu\text{P80 cell volume} = 15 \text{ mm x } 12.6 \text{ mm diameter}$$

5) Battery Packaging

use packaging depicted in Figure E.2

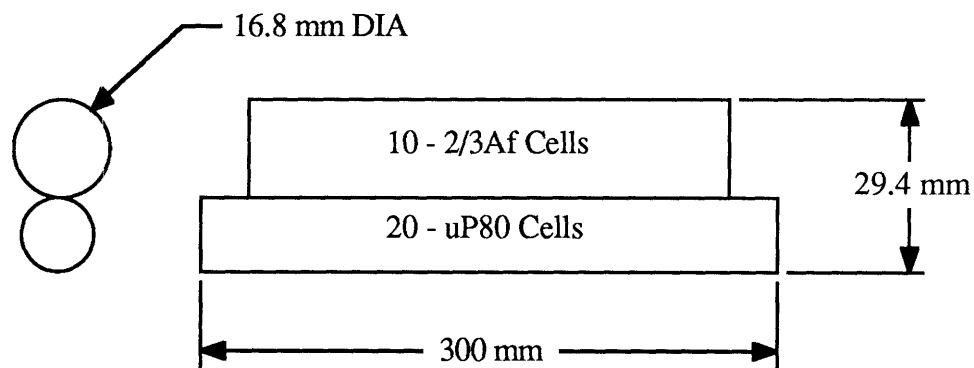overall size: 29.4 mm height

300 mm length

16.8 mm wide

Figure E.2: Battery Packaging.